Research Article

Myosin-driven Nucleation of Actin Filaments Drives Stereocilia Development Critical for Hearing

Zane G. Moreland[#1,2,3], Fangfang Jiang[#1,2], Carlos Aguilar[#4], Melanie Barzik[#5], Rui Gong[7], Arik Shams[5], Christian Faaborg-Andersen[5], Jesse C. Werth[5], Randall Harley[5], Daniel C. Sutton[5], Stacey M. Cole[5], Andrew Parker[4], Susan Morse[4], Elizabeth Wilson[5], Yasuharu Takagi[6], James R. Sellers[6], Steve D.M. Brown[4], Thomas B. Friedman[5], Gregory M. Alushin[7], Michael R. Bowl[4,8]* & Jonathan E. Bird[1,2]*

[1]Department of Pharmacology and Therapeutics, and [2]Myology Institute, and [3]Graduate Program in Biomedical Sciences, University of Florida, Gainesville, FL 32610, USA. [4]Mammalian Genetics Unit, MRC Harwell Institute, Harwell Campus, OX11 0RD, UK. [5]Laboratory of Molecular Genetics, National Institute on Deafness and Other Communication Disorders, National Institutes of Health, Bethesda, MD 20814, USA. [6]Laboratory of Molecular Physiology, National Heart, Lung and Blood Institute, National Institutes of Health, Bethesda, MD 20814, USA. [7]Laboratory of Structural Biophysics and Mechanobiology, The Rockefeller University, New York, NY 10065, USA. [8]UCL Ear Institute, University College London, 332 Gray's Inn Road, London, WC1X 8EE, UK

[#]Authors contributed equally

*Co-corresponding authors

Lead contact: j.bird@ufl.edu

Running title: A myosin motor regulates actin polymerization

Keywords: Actin, myosin, hearing, deafness, hair cell, stereocilia, molecular motor, MYO15, DFNB3

SUMMARY

The assembly and maintenance of actin-based mechanosensitive stereocilia in the cochlea is critical for lifelong hearing. Myosin-15 (MYO15) is hypothesized to modulate stereocilia height by trafficking actin regulatory proteins to their tip compartments, where actin polymerization must be precisely controlled during development. We identified a mutation (p.D1647G) in the MYO15 motor-domain that initially maintained trafficking, but caused progressive hearing loss by stunting stereocilia growth, revealing an additional function for MYO15. Consistent with its maintenance of tip trafficking *in vivo*, purified p.D1647G MYO15 modestly reduced actin-stimulated ATPase activity *in vitro*. Using ensemble and single-filament fluorescence *in vitro* assays, we demonstrated that wild-type MYO15 directly accelerated actin filament polymerization by driving nucleation, whilst p.D1647G MYO15 blocked this activity. Collectively, our studies suggest direct actin nucleation by MYO15 at the stereocilia tip is necessary for elongation *in vivo*, and that this is a primary mechanism disrupted in DFNB3 hereditary human hearing loss.

INTRODUCTION

Cochlear hair cells are the primary transducers of sound in the mammalian inner ear and are fundamental for hearing. Each hair cell assembles approximately 100 individual stereocilia on its apical surface to form a mechano-sensitive hair bundle. Within each bundle, stereocilia are precisely graded into ranks of ascending height and this staircase architecture is critical for mechano-electric transduction (MET) (Barr-Gillespie, 2015). The regulation of stereocilia size is thus central for hearing and the disruption of hair bundle architecture is a common theme in hereditary deafness (Richardson et al., 2011). Stereocilia develop from microvilli by building a highly cross-linked para-crystalline core of actin filaments as an internal scaffold to confer shape and structural rigidity (Vélez-Ortega and Frolenkov, 2019). As stereocilia develop, the actin core thickens and elongates to reach its mature size, necessitating precise control of actin filament polymerization (Tilney et al., 1992; Kaltenbach et al., 1994; Krey et al., 2020). Actin filaments are uniformly polarized within stereocilia with rapidly growing barbed ends orientated towards the tip, the major site of actin polymerization and filament elongation, and also the site of MET (Flock and Cheung, 1977; Tilney et al., 1980; Beurg et al., 2009). Once stereocilia are fully assembled, actin polymerization continues primarily at the tip compartment, indicating an ongoing plasticity throughout adult life (Schneider et al., 2002; Zhang et al., 2012; Drummond et al., 2015; Narayanan et al., 2015). A number of proteins have been identified within the tip compartment that are essential for stereocilia growth, yet the molecular mechanisms governing actin polymerization are unknown. Identification of this mechanism is central to the acquisition and maintenance of hair cell mechano-sensitivity, and also for understanding hearing loss as the clinical manifestation of a cytoskeletal disease.

A key molecule in establishing stereocilia architecture is unconventional myosin 15 (MYO15), encoded by the gene *Myo15* in mice and *MYO15A* in humans. Mutations in *MYO15A* (MIM #602666) cause DFNB3 recessive hereditary hearing loss in humans (Friedman et al., 1995; Wang et al., 1998; Rehman et al., 2016). MYO15 is a member of the myosin superfamily of P-loop ATPases that generate contractile force on actin filaments to power cellular processes such as cytokinesis, endocytosis and vesicular trafficking (Hartman and Spudich, 2012; Houdusse and Sweeney, 2016). Two MYO15 isoforms are produced in auditory hair cells through alternative mRNA splicing (Liang et al., 1999; Anderson et al., 2000; Fang et al., 2015). A shorter isoform (MYO15-2, also known as MYO15-S) consists of the ATPase ‘motor domain’ and three light chain binding sites that associate with calmodulin-like proteins, in addition to myosin tail homology 4 (MyTH4), Src homology 3 (SH3), and protein 4.1, ezrin, radixin, moesin (FERM) domains (Fig. 1A). A larger isoform (MYO15-1, also known as MYO15-L) is identical to MYO15-2, except for the addition of a 133 kDa N-terminal domain

79 (Fig. 1A). Both MYO15 isoforms localize to the stereocilia tip compartment where actin polymerization
80 is concentrated (Schneider et al., 2002; Belyantseva et al., 2003; Drummond et al., 2015; Fang et al.,
81 2015; Narayanan et al., 2015). The prototypical *Myo15* mutant allele, the *shaker 2* (*Myo15*^{sh2}),
82 prevents both isoforms from accumulating in stereocilia, blocking developmental elongation and
83 causing profound hearing loss from birth (Probst et al., 1998; Anderson et al., 2000; Belyantseva et
84 al., 2003; Fang et al., 2015). The use of an isoform-specific *Myo15* null allele revealed additional
85 functions, with MYO15-2 being necessary for stereocilia developmental elongation, whilst MYO15-1
86 independently maintains the postnatal size of shorter stereocilia (Fang et al., 2015) that are
87 structurally plastic in response to MET (Vélez-Ortega et al., 2017; Krey et al., 2020).
88
89 The MYO15-2 isoform associates with additional proteins essential for stereocilia elongation,
90 and by inference, actin polymerization. The 'elongation complex' consists of epidermal growth factor
91 receptor pathway substrate 8 (EPS8), whirlin (WHRN), G-protein signalling modulator 2 (GPSM2) and
92 G-protein subunit alpha$_{i3}$ (GNAI3). Similar to MYO15-2, these proteins are concentrated at the tips of
93 the tallest stereocilia (row 1) (Mburu et al., 2003; Belyantseva et al., 2005; Delprat et al., 2005; Manor
94 et al., 2011; Zampini et al., 2011; Tarchini et al., 2016; Mauriac et al., 2017; Tadenev et al., 2019).
95 Individual knock-out mouse mutants of *Eps8*, *Whrn*, *Gpsm2* or *Gnai3* recapitulate the *shaker 2*
96 phenotype, exhibit short stereocilia and are profoundly deaf (Mburu et al., 2003; Manor et al., 2011;
97 Zampini et al., 2011; Tarchini et al., 2016; Mauriac et al., 2017; Tadenev et al., 2019). There is strong
98 evidence that a key function of MYO15-2 is to traffic the elongation complex and concentrate it at the
99 stereocilia tips. First, elongation complex proteins are absent from the stereocilia of *Myo15 shaker 2*
100 hair cells, demonstrating their functional dependence upon MYO15-2 *in vivo* (Belyantseva et al., 2005;
101 Delprat et al., 2005; Manor et al., 2011; Mauriac et al., 2017; Tadenev et al., 2019). Second, EGFP-
102 tagged MYO15-2 actively traffics elongation complex proteins along filopodia in cell lines (Belyantseva
103 et al., 2005; Manor et al., 2011; Mauriac et al., 2017). Finally, enzymatic studies of the purified MYO15
104 ATPase domain reveal kinetic adaptations that enable long-range processive molecular trafficking
105 (Bird et al., 2014; Jiang et al., 2021). Together, these data support MYO15-2 delivering the elongation
106 complex to the stereocilia tips, where the elongation complex is hypothesized to regulate actin
107 polymerization. Despite its central role in promoting stereocilia growth, the specific molecular activity
108 of the elongation complex remains unknown.
109
110 Here, we describe a novel *Myo15* mutant mouse ('*jordan*') that exhibits progressive hearing
111 loss resulting from a missense substitution in the MYO15 motor domain. In striking contrast with
112 *shaker 2* hair cells, MYO15 and the elongation complex proteins are still delivered to the stereocilia tip

113 compartment in *jordan* mutant hair cells, but stereocilia fail to elongate properly. These results
114 questioned the sufficiency of the elongation complex to drive stereocilia growth, and prompted us to
115 search for another role of MYO15 independent of delivering the elongation complex. We found that
116 purified MYO15 motor domain protein directly stimulated actin polymerization *in vitro*, and that the
117 *jordan* mutation blocked this activity, whilst only moderately affecting its ability to bind and move along
118 actin filaments. A companion structural study shows that the *jordan* mutation targets the actomyosin
119 binding interface and interferes with the ability of wild-type MYO15 to regulate structural plasticity
120 within the actin molecule itself (Gong et al., 2021). Combined, our results argue that MYO15 controls
121 stereocilia elongation by directly regulating F-actin conformation in stereocilia, and that this critical
122 activity is independent of the elongation complex. More broadly, our work suggests that in addition to
123 their classical roles generating force and motility, myosin motors have a physiological role regulating
124 actin polymerization *in vivo*.
125
126 **RESULTS**
127 **A forward genetic screen identifies *jordan,* a *Myo15* allele causing progressive hearing loss**
128 During a recent phenotype-driven ENU-mutagenesis screen (Potter et al., 2016), the MPC190
129 cohort (comprising 83 mice) was identified with 10 mice exhibiting severe hearing loss at 3-months of
130 age (Fig. 1B). A genome scan and single nucleotide polymorphism (SNP) mapping of third generation
131 (G3) deaf mice found linkage to a 16.7 Mb region on Chromosome 11 (Fig. S1A). Whole-genome
132 sequencing of a single deaf mouse identified a high confidence homozygous mutation within the
133 critical interval, consisting of an A-to-G transition at coding nucleotide 4940 of the *Myo15* gene
134 (ENSMUST00000071880). This variant was confirmed by Sanger sequencing (Fig. S1B) and leads to
135 the substitution of an evolutionarily conserved aspartate residue with a glycine (p.D1647G) in the
136 encoded MYO15 protein (Fig. 1C). We named this mutant allele *jordan* ($Myo15^{jd}$).
137
138 To confirm that the $Myo15^{jd}$ substitution causes hearing loss, we performed a genetic
139 complementation test utilizing the *shaker-2* ($Myo15^{sh2}$) deafness allele *in trans* (Probst et al., 1998;
140 Stepanyan et al., 2006). We recorded ABRs from postnatal day 28 (P28) mice and found that
141 compound heterozygous $Myo15^{jd/sh2}$ mice had elevated thresholds of >90 decibel sound pressure level
142 (dB SPL) at all frequencies (Fig. 1D). In contrast, $Myo15^{jd/+}$ and $Myo15^{sh2/+}$ littermates had normal
143 thresholds (< 40 dB SPL) (Fig. 1D). Failure of complementation in $Myo15^{jd/sh2}$ mice confirms that the
144 p.D1647G mutation in *Myo15* is the cause of recessive deafness in the *jordan* pedigree.
145

146 All reported mutant *Myo15* mouse alleles cause profound deafness (MGI:1261811), measured
147 from P14 onwards (Probst et al., 1998; Anderson et al., 2000; Stepanyan et al., 2006; Fang et al.,
148 2015). ABR showed that several *Myo15*$^{jd/jd}$ mice had residual hearing at 3 months (Fig. 1B, red
149 circles), suggesting a distinct mechanism of hearing loss. We investigated this using longitudinal ABR
150 measurements. At 4 weeks of age, *Myo15*$^{jd/jd}$ mice had moderate hearing loss with broadband click
151 ABR threshold of 53 ± 11 dB SPL, compared to normal hearing *Myo15*$^{+/+}$ (26 ± 6 dB SPL) and
152 *Myo15*$^{+/jd}$ (24 ± 6 dB SPL) littermates (Fig. 1E). The hearing of *Myo15*$^{jd/jd}$ mice progressively worsened,
153 with click ABR thresholds of 53 ± 11, 69 ± 9, 80 ± 9 and 81 ± 8 dB SPL at 4, 6, 9 and 12 weeks,
154 respectively (Fig. 1E,F, Fig. S1C-F). Click ABR thresholds for control *Myo15*$^{+/+}$ and *Myo15*$^{jd/+}$
155 littermates ranged between 22 ± 4 and 26 ± 6 dB SPL; showing they did not develop hearing loss with
156 age (Fig. 1E,F, Fig. S1C-F). To investigate outer hair cell (OHC) function we measured distortion-
157 product otoacoustic emissions (DPOAEs), and found they were absent in *Myo15*$^{jd/jd}$ mice at 12 weeks,
158 except for frequencies < 10 kHz, where they were significantly reduced compared to *Myo15*$^{+/+}$ and
159 *Myo15*$^{+/jd}$ littermates (Fig. S1G). The absence of DPOAEs shows that OHC function is impaired in
160 *Myo15*$^{jd/jd}$ mice. As the only known mouse *Myo15* variant to cause progressive hearing loss, the *jordan*
161 allele is an important new model to explore the full spectrum of DFNB3 deafness, which presents
162 heterogeneously as either profound congenital, or progressive hearing loss in humans (Rehman et al.,
163 2016).
164
165 **Stereocilia do not properly elongate in *jordan* mutant hair cells**
166 To investigate the cellular pathology underlying hearing loss in *Myo15*$^{jd/jd}$ mice, we used
167 scanning electron microscopy (SEM) to assess the structure of cochlear hair bundles. In wild-type
168 *Myo15*$^{+/+}$ IHCs and OHCs at P8, stereocilia were graded into a staircase pattern with three distinct
169 rows (Fig. 2A,B). By comparison, bundle heights were reduced in *Myo15*$^{jd/jd}$ littermates, whilst still
170 retaining the staircase architecture (Fig. 2C,D). Quantification of row 1 stereocilia heights showed that
171 *Myo15*$^{jd/jd}$ IHCs and OHCs were significantly shorter than *Myo15*$^{+/+}$ controls (Fig. 2G,H). Furthermore,
172 stereocilia at the lateral edge of *Myo15*$^{jd/jd}$ OHCs, and to lesser extent IHCs, were shorter in height
173 such that the central stereocilia were tallest (Fig. 2C,D). *Myo15*$^{jd/jd}$ hair cells consistently had 1 or 2
174 additional rows of stereocilia (Fig. 2C,D) when compared to the three well-defined rows in *Myo15*$^{+/+}$
175 hair cells (Fig. 2A,B). The additional row phenotype of *Myo15*$^{jd/jd}$ hair cells was similar to *Myo15*$^{sh2/sh2}$
176 hair cells at P8 (Fig. 2E,F), however *Myo15*$^{jd/jd}$ stereocilia lengths were significantly longer when
177 compared to *Myo15*$^{sh2/sh2}$ hair cells (Fig. 2G,H). We conclude that stereocilia in *Myo15*$^{jd/jd}$ hair cells
178 elongate more than *Myo15*$^{sh2/sh2}$ hair cells, but fail to reach normal wild-type heights. The *Myo15*

179 *shaker 2* and *jordan* allelic series shows that mutations in the motor domain led to altered stereocilia
180 heights and explain why *jordan* mice initially have less severe hearing loss than *shaker-2* mice.
181
182 To further investigate the progressive component of hearing loss, we next examined hair
183 bundle morphology at 12 weeks, when *jordan* mice were profoundly deaf (Fig. 1F). Compared with
184 *Myo15*$^{+/+}$, IHC bundles of *Myo15*$^{jd/jd}$ mice had lost their staircase architecture (Fig. S2A) and were still
185 significantly shorter (Fig. S2B). Since the staircase was initially present at P8 in *Myo15*$^{jd/jd}$ IHCs (Fig.
186 2D), these data suggested a postnatal resorption of stereocilia. Consistent with this hypothesis,
187 extremely short stereocilia at the hair bundle periphery were observed at 12 weeks in *Myo15*$^{jd/jd}$ OHCs
188 (Fig. S2C,D). These data argue that the progressive hearing phenotype in the *jordan* mouse was due
189 to postnatal stereocilia bundle degradation. Overall, we conclude that the *jordan* allele causes hearing
190 loss by interfering with both initial elongation of stereocilia, and their postnatal maintenance. This was
191 consistent with the p.D1647G mutation targeting the motor domain of both MYO15 isoforms (Fang et
192 al., 2015).
193
194 **MYO15 traffics the elongation complex in *jordan* hair cells**
195 Hair bundle development requires MYO15 dependent trafficking of EPS8, WHRN, GNAI3 and
196 GPSM2 (the 'elongation complex'), and mutations that prevent MYO15 trafficking (*i.e. shaker-2*) cause
197 a short hair bundle phenotype (Belyantseva et al., 2005; Manor et al., 2011; Mauriac et al., 2017;
198 Tadenev et al., 2019). Our finding that stereocilia lengths in the *jordan* mouse were only marginally
199 longer than the *shaker-2*, led us to hypothesize that MYO15 trafficking was defective in *jordan* hair
200 cells. We used the previously validated pan-MYO15 antibody PB48 (Fig. 1A), that binds an epitope
201 common to all isoforms (Liang et al., 1999; Fang et al., 2015), to detect MYO15 in fixed cochleae from
202 *Myo15*$^{jd/jd}$ mutants and *Myo15*$^{+/jd}$ littermates at P14. As expected, in *Myo15*$^{+/jd}$ mice, PB48 labelling
203 was concentrated at the tips of all stereocilia rows in IHCs (Fig. 3A) (Belyantseva et al., 2003, 2005;
204 Rzadzinska et al., 2004). We confirmed that PB48 did not label the short stereocilia of *Myo15*$^{sh2/sh2}$
205 IHCs at P14 (Fig. 3A), consistent with MYO15 being absent from the bundle (Belyantseva et al.,
206 2003). In stark contrast with the *shaker-2*, we observed PB48 labelling at the tips of IHC stereocilia in
207 *Myo15*$^{jd/jd}$ mice at both P7 and P14 (Fig. 3A,B). These data support the *jordan* and *shaker-2* mutations
208 affecting stereocilia growth by profoundly different mechanisms: the *shaker-2* mutation blocks MYO15
209 trafficking, whilst the *jordan* mutation allows MYO15 to traffic but prevents stereocilia elongation.
210
211 We next investigated if the *jordan* mutation interfered with trafficking of the elongation complex
212 proteins. To test this, mutant *Myo15*$^{jd/jd}$ and control *Myo15*$^{+/jd}$ littermate cochleae at P7 were labelled

213 with validated antibodies to localize WHRN, EPS8, GPSM2 and GNAI3. All of the elongation complex
214 proteins were concentrated at the tips of the tallest stereocilia (row 1) in control *Myo15*$^{+/jd}$ hair cells
215 (Fig. 3C), in agreement with previous work (Mburu et al., 2003; Manor et al., 2011; Zampini et al.,
216 2011; Tarchini et al., 2016; Mauriac et al., 2017). All four proteins in the elongation complex were also
217 targeted to the stereocilia tips in mutant *Myo15*$^{jd/jd}$ hair cells (Fig. 3C), although the signal-to-noise of
218 GPSM2 and GNAI3 was lower, indicating a reduced overall accumulation (Fig. 3C). In older animals at
219 P14, EPS8 and WHRN were still correctly targeted in *Myo15*$^{jd/jd}$ hair cells, however GNAI3 and
220 GPSM2 were no longer concentrated at stereocilia tips (Fig. S3). These data are consistent with
221 GPSM2-GNAI3 operating as a distinct complex with MYO15-EPS8 (Tadenev et al., 2019). We
222 conclude that the initial defective stereocilia elongation in *jordan* hair cells evident at P7 was not due
223 to gross disruption of elongation complex trafficking by MYO15.
224
225 **Actin barbed end capping is unaffected in *jordan* mutant hair cells**
226 The presence of the elongation complex at the stereocilia tips of *jordan* hair cells suggested
227 that the proteins known to stimulate growth were present, but insufficient to drive elongation. We
228 considered whether an overall inhibition of actin polymerization was preventing stereocilia elongation
229 in *jordan* hair cells. Capping proteins (CAPZ, TWF2) are present within stereocilia and regulate
230 filament polymerization by blocking barbed end elongation (Peng et al., 2009; Avenarius et al., 2017).
231 To detect free barbed ends, we monitored the incorporation of TMR-labelled actin monomers in
232 permeabilized hair cells at P6. In control *Myo15*$^{+/jd}$ hair cells, TMR-actin was concentrated at row 2
233 stereocilia tips revealing uncapped barbed ends (Fig. 4A). TMR-actin was not consistently detected at
234 row 1 tips, arguing that barbed ends were inaccessible at that location (Fig. 4A). The *jordan* mutation
235 did not alter this distribution of free barbed ends and we observed a similar incorporation of TMR-actin
236 in *Myo15*$^{jd/jd}$ hair cells compared to controls (Fig. 4A). In striking contrast, TMR-actin was incorporated
237 at the tips of all stereocilia rows in *Myo15*$^{sh2/sh2}$ hair cells, indicating the abnormal presence of barbed
238 ends in row 1, and an overall loss of hair bundle row identity (Fig. 4A). In summary, *jordan* hair cells
239 retain row identity at P6, consistent with MYO15 correctly targeting the elongation complex to the
240 stereocilia tip compartment. These data argue that inappropriate actin filament capping is unlikely the
241 cause of short stereocilia in *jordan* hair cells. Instead, we hypothesized that a stimulatory factor
242 independent of the elongation complex was missing.
243
244 **The *jordan* mutation affects the interaction of MYO15 with actin filaments**
245 The *jordan* missense substitution is in the MYO15 motor domain helix-loop-helix (HLH) motif
246 that forms part of the direct binding interface with the actin filament (Gong et al., 2021). We

247 hypothesized that a defect in MYO15's interaction with actin might underlie the *jordan* phenotype. To
248 explore this, we examined MYO15-2 trafficking along filopodia; actin-based structures that protrude
249 from the periphery of heterologous cells (Belyantseva et al., 2003, 2005). We focused on MYO15-2 as
250 the isoform responsible for stereocilia growth (Fang et al., 2015). In transfected HeLa cells, EGFP-
251 tagged wild-type MYO15-2 accumulated at filopodia tips indicating robust anterograde myosin
252 movement along the filopodia shaft (Fig. 4B). Discrete puncta of MYO15-2 were observed along the
253 filopodia shaft, arising from retrograde actin filament treadmilling (Belyantseva et al., 2005; Kerber et
254 al., 2009; Bird et al., 2017). EGFP alone did not accumulate within filopodia, proving this distribution
255 required active myosin motility (Fig. 4B). In cells expressing the MYO15-2 *jordan* mutant, EGFP was
256 observed diffusely along filopodia shafts and was not concentrated at filopodia tips (Fig. 4B). This was
257 qualitatively similar to cells expressing the MYO15-2 *shaker-2* mutant (Fig. 4B), which was previously
258 shown to not traffic along filopodia (Belyantseva et al., 2005). The inability of the MYO15-2 *jordan*
259 mutant to traffic within filopodia and accumulate at filopodia tips was unexpected and contrary to
260 MYO15 protein accumulating at the stereocilia tips of *Myo15*$^{jd/jd}$ hair cells (Fig. 3A).
261
262 Myosin motors are sensitive to actin filament topology (Nagy et al., 2008; Brawley and Rock,
263 2009; Reymann et al., 2012; Ropars et al., 2016) and we hypothesized that filopodia might not contain
264 the appropriate repertoire of actin-binding proteins (ABPs) to support motility. To test this hypothesis,
265 we used the porcine LLC-PK1-CL4 (CL4) epithelial cell line that generates microvilli and is a more
266 accurate model for stereocilia (Zheng et al., 2010). In CL4 cells transfected with wild-type EGFP-
267 MYO15-2, EGFP positive puncta localized at the tips of microvilli (Fig. 4C, orthogonal projections). In
268 striking contrast to HeLa cells, the MYO15-2 *jordan* mutant also concentrated into microvilli and was
269 indistinguishable from the wild-type in CL4 cells (Fig. 4C). No microvillar accumulation of the MYO15-
270 2 *shaker-2* mutant was observed (Fig. 4C). We conclude that whilst *jordan* and *shaker-2* mutants are
271 both immobile within filopodia, the *jordan* mutant can still actively concentrate in microvilli. These data
272 mimic our findings from hair cells *in vivo*, and support a change in actin binding as being central to the
273 stereocilia growth defect phenotype observed in *jordan* hair cells.
274
275 **The ATPase activity of MYO15 is altered by the *jordan* mutation**
276 To study the interaction between MYO15 and actin filaments in more detail, we characterized
277 the influence of the *jordan* mutation upon ATPase mechanochemistry (Bird et al., 2014; Jiang et al.,
278 2021). Motor domain proteins were expressed in *S. frugiperda* (*Sf*9) insect cells and purified by
279 chromatography (Fig. 5A,C). In contrast to the *shaker-2* variant, which aggregated within *Sf*9 cells,
280 both wild-type and *jordan* motor domains were soluble. Using size exclusion chromatography (SEC),

281 we found that FLAG-purified *shaker-2* motor domain eluted close to the void volume (Fig. 5B). In
282 contrast, the *jordan* motor domain eluted at a similar delay volume to the wild-type (Fig. 5B), which is
283 monomeric (Bird et al., 2014). We conclude that the *jordan* variant does not affect folding, whilst the
284 *shaker-2* caused misfolding, consistent with the mutation being within the ATPase transducer core
285 (Gong et al., 2021).
286
287 To test for differences in enzymatic activity between wild-type and *jordan* motor domain
288 variants (Fig. 5A), we measured steady-state ATP hydrolysis using an enzyme-linked NADH assay.
289 The basal ATPase activity (k_{basal}) of the wild-type motor domain was 0.06 ± 0.01 s^{-1}, measured without
290 F-actin. The addition of F-actin caused a 97-fold increase in ATPase activity to an extrapolated
291 maximum catalytic rate (k_{cat}) of 5.8 ± 0.2 s^{-1} (Fig. 5D). Half-maximal activation of the ATPase activity
292 (K_{ATPase}) was reached at 29.1 ± 2.1 μM F-actin, as previously reported (Bird et al., 2014; Jiang et al.,
293 2021). Using identical assay conditions, the basal ATPase rate of the *jordan* variant was unchanged at
294 k_{basal} = 0.07 ± 0.01 s^{-1}. Strikingly, there was a reduced 7-fold maximal activation to k_{cat} = 0.87 ± 0.04 s^{-1}
295 (Fig. 5D). Furthermore, half-maximal ATPase activation was increased to K_{ATPase} = 114.3 ± 8.2 μM
296 actin, signifying a 4-fold reduction in the apparent actin affinity compared to wild-type.
297
298 The mechanical activity of wild-type and *jordan* motor domains was measured using an *in vitro*
299 gliding filament assay, where actin filaments are propelled across a microscope cover glass
300 functionalized with motor domain protein (Sellers et al., 1993). Due to the reduced apparent affinity of
301 the *jordan* motor domain for actin, we lowered the salt concentration to 10 mM KCl in these assays.
302 The wild-type motor domain robustly propelled actin filaments at 473 ± 67 nm·s^{-1} (Fig. 5E), consistent
303 with previous data (Bird et al., 2014). In contrast, the *jordan* mutant moved filaments at 216 ± 71 nm·s^{-}
304 ^{1}, a 2-fold reduction from the wild-type velocity (Fig. 5E). Overall, we conclude that whilst the *jordan*
305 mutation caused a significant ATPase defect and decreased the motor domain's apparent affinity for
306 actin, the motor domain was still mechanically active. Our data further establish a functional
307 correlation between motor domain activity and the severity of hearing loss in a *Myo15* allelic series.
308 The *jordan* motor domain retained partial activity consistent with this mutation causing intermediate
309 hearing loss, whilst the *shaker-2* motor domain was misfolded and associated with the most severe
310 phenotype.
311
312 **The MYO15 motor domain directly stimulates actin polymerization**
313 Our *in vitro* analysis of purified MYO15 motor activities were consistent with the *jordan* mutant
314 maintaining the ability to traffic the elongation complex and accumulate at stereocilia tips. As

315 stereocilia nevertheless fail to grow normally in *jordan* hair cells, we hypothesized that independent of
316 molecular trafficking, MYO15 had an additional function at the stereocilia tip critical for elongation.
317 Classic biochemical studies of muscle myosin have shown its motor domain (*e.g.* subfragment-1, S1)
318 can directly stimulate actin polymerization *in vitro*; however, the physiological relevance of this activity
319 *in vivo*, if any, is unknown (Yagi et al., 1965; Miller et al., 1988; Fievez and Carlier, 1993; Lheureux et
320 al., 1993). We hypothesized that the MYO15 motor domain could directly stimulate actin
321 polymerization to drive stereocilia elongation, and that this critical activity is disrupted by the *jordan*
322 deafness mutation.
323
324 We tested this hypothesis using pyrene-conjugated globular actin (G-actin) monomers that
325 increase in fluorescence as they polymerize into filamentous actin (F-actin) (Cooper et al., 1983). As a
326 control, 2 μM G-actin was polymerized with 1x KMEI (50 mM KCl, 1 mM $MgCl_2$, 1 mM EGTA, 10 mM
327 imidazole) while monitoring pyrene fluorescence. F-actin assembled with an initial lag phase
328 representing the kinetically unfavourable nucleation step (Fig. 6A, red line). When the reaction was
329 repeated with 1 μM wild-type motor domain + 2 μM G-actin + KMEI, actin polymerization initially
330 followed the same trajectory (Fig. 6A, blue line). However, following a delay of ~ 400 seconds, an
331 inflection was observed where the rate of actin polymerization reduced momentarily (Fig. 6A, blue
332 line), before rapidly increasing and reaching steady-state (Fig. 6A,B). We tested if MYO15-stimulated
333 actin polymerization was sensitive to the *jordan* mutation. Under identical experimental conditions
334 using 1 μM *jordan* MYO15 motor domain, the actin polymerization rate was initially indistinguishable
335 from the control reaction. However, following an inflection at ~ 600 seconds, the actin polymerization
336 rate decreased below that of the G-actin alone control (Fig. 6A). We conclude that the wild-type
337 MYO15 motor domain stimulated actin polymerization, whilst the deafness-causing *jordan* mutant
338 blocked this activity.
339
340 With either wild-type or *jordan* motor domains, we observed a delay before the actin
341 polymerization rate deviated from the control, with the delay longer for *jordan* (~ 600s) versus wild-
342 type (~ 400s). We hypothesized this difference arose from residual ATP (70 μM) being introduced
343 from the G-actin storage buffer; ATP binding would prevent the motor domain from occupying the
344 strongly actin bound (rigor) state. Furthermore, we expected this residual ATP to be hydrolysed faster
345 by the wild-type motor domain, compared with the *jordan* mutant (Fig. 5D). To test this, we repeated
346 the pyrene polymerization assay in the absence of free ATP. To ensure G-actin monomers were ATP-
347 bound, G-actin was desalted immediately prior to use to remove free ATP from solution. Using this
348 approach, we measured the polymerization of 2 μM G-actin + KMEI in the absence of free ATP (Fig.

349 6C) and observed kinetics comparable to before (Fig. 6A). Strikingly, pyrene fluorescence immediately
350 increased upon addition of 1 μM wild-type motor to the reaction, and rapidly saturated (Fig. 6C) with a
351 significantly reduced half-time of 124 ± 12 s, compared with 1091 ± 202 s for G-actin + KMEI alone
352 (Fig. 6D). While addition of 1 μM *jordan* motor domain to 2 μM G-actin + KMEI reduced the overall
353 extent of actin polymerization (Fig. 6C), the half-time to saturation was 1000 ± 65 s and not
354 significantly different to G-actin + KMEI alone (Fig. 6D). We conclude that the wild-type MYO15 motor
355 domain strongly accelerated actin filament polymerization in the absence of ATP, implicating the rigor
356 state as critical for this activity. Combined with experiments from our companion study showing that
357 ADP-bound MYO15 also stimulated polymerization (Gong et al., 2021), these data identify the strong
358 actin-binding states as the key MYO15 ATPase intermediates that stimulate actin polymerization.
359
360 **The *jordan* deafness mutation inhibits *de novo* nucleation of actin filaments**
361 To directly visualize how the MYO15 motor domain accelerates polymerization, we performed
362 actin polymerization assays using total internal reflection fluorescence microscopy (TIRFM) where the
363 elongation of individual filaments can be tracked (Fujiwara et al., 2002). A control time-lapse of 1 μM
364 G-actin + KMEI revealed a slow rate of filament nucleation, with short polymers attaching to surface
365 and elongating (Fig. 7A, top row). We repeated the experiment with 1 μM wild-type motor domain and
366 observed a large burst in filament density (Fig. 7A, middle row) that was statistically significant at 480
367 seconds when compared to the actin-alone control (Fig. 7B). In contrast, when polymerization
368 experiments were repeated with 1 μM *jordan* motor domain (Fig. 7A, bottom row), there was no
369 increase in actin filament density above the actin-alone control (Fig. 7C). Using kymographs to track
370 filament barbed ends, we found that the motor domain could influence actin filament elongation rates.
371 In control experiments, barbed ends elongated at 16.2 ± 2.6 $nm \cdot s^{-1}$ (Fig. 7C,D), consistent with
372 previous data using TMR-conjugated G-actin on Cys374 (Kuhn and Pollard, 2005). Elongation rates
373 were significantly reduced by the addition of either wild-type or *jordan* motor domain, to 13.3 ± 4.3
374 $nm \cdot s^{-1}$ and 13.4 ± 3.5 $nm \cdot s^{-1}$, respectively (Fig. 7C,D). The decrease in elongation rate was dependent
375 upon timing of the filament burst (Fig. 7B). When data were binned as pre-burst (< 320 s), the addition
376 of wild-type or *jordan* motor domains did not significantly alter elongation rates compared to the
377 control (Fig. 7E). In contrast, the presence of either wild-type or *jordan* motor domain post-burst (> 720
378 s) both significantly, and equally, reduced elongation rates below the actin alone control (Fig. 7F).
379
380 Nucleation by wild-type MYO15 took an average of 480 seconds to be significantly increased
381 above the spontaneous nucleation rate of G-actin + KMEI alone (Fig. 7B). We considered whether the
382 delayed production of short filaments was caused by MYO15 severing actin filaments that nucleated

383 spontaneously. To test this hypothesis, we repeated our experiments in the absence of free ATP to
384 force the motor domain into rigor binding and accelerate polymerization. Free ATP was desalted from
385 1 μM G-actin monomers; this did not affect barbed-end elongated rates when polymerized by KMEI
386 (Fig. 7D,I). As expected, when 1 μM wild-type motor domain was included in the reaction, there was a
387 potent nucleation of short actin filaments observed within 90 s (Fig. 7G,H), confirming acceleration of
388 nucleation when the motor domain was forced into rigor. Under identical ATP free conditions, 1 μM
389 *jordan* motor domain did not nucleate additional filaments compared with the G-actin + KMEI control
390 (Fig. 7G,H). Similar to experiments where ATP was present, but presumably hydrolyzed (Fig. 7F, >
391 720 s), we saw that both wild-type and *jordan* motor domains significantly reduced barbed-end
392 elongation rates (Fig. 7I). We conclude that the MYO15 motor domain exerts multiple direct effects on
393 actin polymerization, including catalyzing *de novo* filament nucleation and reducing barbed end
394 elongation rates in a nucleotide-dependent fashion. Our data show that MYO15-induced actin
395 nucleation is a key process targeted by the *jordan* deafness mutation, and argue that this activity is
396 critical for stereocilia elongation and hearing.
397
398 **DISCUSSION**
399 Plasticity of the stereocilia actin core is central to hair bundle development, mechano-
400 sensitivity and hearing. Existing evidence that MYO15 moves along stereocilia actin filaments has led
401 to a cargo trafficking model, where the elongation complex is delivered to the stereocilia tips and
402 provides the actin regulation machinery necessary for elongation. Here, we uncover a previously
403 unknown activity of MYO15 that requires the cargo-trafficking model to be re-evaluated. *In vitro*, we
404 show that MYO15 can directly stimulate actin filament nucleation and that this activity is inhibited by
405 the *jordan* mutation, providing key evidence this activity is functionally linked to deafness pathology. *In*
406 *vivo*, the *Myo15 jordan* mutation stunted stereocilia growth, leading to an early-onset, progressive
407 hearing loss in mice. The effect of the *jordan* mutation to inhibit MYO15-induced actin nucleation *in*
408 *vitro*, and block stereocilia elongation *in vivo*, provides the functional link between these two
409 processes. We propose that in addition to trafficking key molecular cargos, MYO15 directly catalyses
410 actin filament nucleation at the stereocilia tip, and that both these processes combined are required
411 for normal stereocilia growth.
412
413 Using purified proteins and reconstituted assays, the MYO15 motor domain exerted multiple
414 effects upon actin filament polymerization *in vitro*. The motor domain: 1) nucleated actin filaments *de*
415 *novo*, and 2) slowed the elongation rate of existing actin filaments. No additional proteins were
416 required, demonstrating that these properties were intrinsic to the purified actomyosin system. The

417 *jordan* mutation completely blocked MYO15-induced actin filament nucleation, whilst filament
418 elongation rates were unaffected relative to wild-type MYO15. We conclude that MYO15's nucleation
419 activity is the key polymerization effect disrupted by the *jordan* deafness mutation. Similar to MYO15,
420 muscle myosin was shown in classic biochemical experiments to stimulate actin filament nucleation *in*
421 *vitro* (Yagi et al., 1965; Miller et al., 1988; Fievez and Carlier, 1993; Lheureux et al., 1993). The
422 MYO15 motor domain shares a common structural fold with muscle myosin (Gong et al., 2021), and
423 although the mechanism of muscle nucleation remains controversial (Lheureux et al., 1993), we
424 believe by homology to muscle that MYO15 nucleates actin through stabilizing inter-subunit contacts
425 that establish the protofilament (Fievez et al., 1997a, 1997b). In our companion study (Gong et al.,
426 2021), the MYO15 motor domain is further shown to influence structural plasticity within the DNaseI-
427 binding loop (D-loop), a sub-domain of actin that regulates the monomer to polymer transition
428 (Dominguez and Holmes, 2011). Combined, our data argue that nucleation is a shared function for at
429 least some members of the myosin superfamily, and that myosin motors can directly influence
430 cytoskeletal plasticity in addition to their canonical role generating force.
431
432 A cellular function for myosin-driven actin nucleation has, to the best of our knowledge, not
433 previously been reported in any tissue. Our study provides evidence that MYO15-driven nucleation
434 contributes to hair cell function *in vivo*, and furthermore is a cause of disease when disrupted. Actin
435 nucleation by MYO15 appears distinct from other nucleation factors, such as formins, Arp2/3, Spire
436 and Cobl (Machesky et al., 1994; Mullins et al., 1997, 1998; Sagot et al., 2002; Quinlan et al., 2005;
437 Ahuja et al., 2007). MYO15-driven nucleation was nucleotide-sensitive, and strongly promoted
438 nucleation under rigor (nucleotide-free) conditions, or when bound to ADP (Gong et al., 2021). Both
439 conditions populate the motor domain into strong actin binding states (Jiang et al., 2021). Conversely,
440 the presence of ATP in assays prevented nucleation and we hypothesize this is due to the motor
441 domain populating a weakly actin-bound state (Jiang et al., 2021). The nucleotide-sensing properties
442 of MYO15 may therefore couple local concentrations of ATP and ADP to actin polymerization. We
443 speculate this activity could form the basis of a tuning mechanism, where dynamic changes in
444 nucleotide concentrations control the height of developing stereocilia. The concentrations of ATP and
445 ADP in stereocilia are unknown, and whilst a creatine kinase ATP generation system has been
446 described in avian hair cells (Shin et al., 2007), its activity in mammals is unclear (Krey and Barr-
447 Gillespie, 2019). In addition to nucleotide state, MYO15-driven nucleation *in vitro* was observed at
448 high protein concentrations equimolar with actin, in agreement with data from muscle myosin (Miller et
449 al., 1988). The concentration of MYO15 in hair cells is unknown, however micromolar quantities may
450 be present at the stereocilia tips, especially as MYO15 actively traffics and self concentrates into this

451 subcellular compartment (Belyantseva et al., 2003). Other unconventional myosin motors critical for
452 hearing, including MYO1C, MYO3A, MYO6 and MYO7A (Avraham et al., 1995; Gibson et al., 1995;
453 Gillespie and Corey, 1997; Hasson et al., 1997; Holt et al., 2002; Salles et al., 2009; Ebrahim et al.,
454 2016), also concentrate in specific stereocilia sub-domains and it is exciting to consider whether they
455 also directly regulate actin polymerization as part of their cellular function.
456
457 In parallel with identifying MYO15 as an actin nucleator, we used the *jordan* mutant mouse to
458 probe sufficiency of the elongation complex to drive stereocilia elongation. Each protein in the
459 elongation complex is critical for growth, but existing models do not explain their molecular activty,
460 except that they must be delivered to the stereocilia tip via MYO15-driven trafficking. This model is
461 based on the *shaker-2* mouse, where stereocilia growth is inhibited and both MYO15 and the
462 elongation complex are absent from the hair bundle (Belyantseva et al., 2005; Delprat et al., 2005;
463 Manor et al., 2011; Zampini et al., 2011; Mauriac et al., 2017; Tadenev et al., 2019). Our data show
464 that MYO15-driven actin nucleation and elongation complex trafficking activities are simultaneously
465 lost in the *shaker-2*, leaving their relative contributions unknown. By contrast, MYO15-driven trafficking
466 of the elongation complex is initially (largely) preserved in the short stereocilia of the *jordan* mouse.
467 These data argue that the elongation complex proteins are necessary, but not sufficient for driving
468 stereocilia growth, and that MYO15-nucleation activity is critical *in vivo*. We cannot exclude the
469 possibility of reduced MYO15 trafficking in *jordan* hair cells; indeed, gliding filament velocities of the
470 mutant motor were ~ 50% of the wild-type *in vitro*. However, there is no evidence that the
471 concentration of MYO15 at the stereocilia tips determines stereocilia length. Neither the elimination of
472 MYO15-1 from shorter stereocilia rows (Fang et al., 2015), nor the over-expression of MYO15-2 alters
473 initial stereocilia lengths (Belyantseva et al., 2003, 2005). We also considered whether the *jordan*
474 mutation might interfere with MYO15 binding to another protein critical for stereocilia growth. Our
475 companion study (Gong et al., 2021) localizes the *jordan* missense substitution to the actomyosin
476 interface, and shows a direct structural effect within the actin monomer itself. Combined with our
477 study, these findings strongly suggest that MYO15 directly accelerates actin nucleation at the
478 stereocilia tip by structurally regulating the actin molecule.
479
480 Our study raises new questions concerning the stability and plasticity of the stereocilia
481 cytoskeleton, processes that must be tightly controlled for mechano-transduction and lifelong hearing
482 (Vélez-Ortega and Frolenkov, 2019). Stereocilia actin filaments are unidirectionally polarized with their
483 fast-growing barbed ends orientated towards the tip compartment, where new actin monomers are
484 incorporated (Flock and Cheung, 1977; Tilney et al., 1980; Schneider et al., 2002; Drummond et al.,

485 2015). Although actin capping proteins also contribute to stereocilia architecture (Peng et al., 2009;
486 Avenarius et al., 2017), we find that excessive barbed end capping is not the cause of short stereocilia
487 in *Myo15* mutant mice. Given the presence of barbed ends, why might actin nucleation be required to
488 extend pre-existing filaments at stereocilia tips? One possible explanation is that stereocilia elongation
489 occurs through direct end-to-end annealing of short actin polymers nucleated by MYO15, rather than
490 through addition of individual actin monomers at the barbed end. Pre-formed actin filaments can
491 anneal into longer filaments *in vitro* (Murphy et al., 1988; Kinosian et al., 1993; Sept et al., 1999), and
492 more recent *in vitro* studies have detected filament extension through incorporation of short polymers,
493 in addition to the dominant mode of monomer addition (Young et al., 2018). Interestingly, endocytosis
494 in yeast is proposed to use end-to-end actin filament annealing rather than monomer polymerization
495 (Okreglak and Drubin, 2010). Though speculative in hair cells, the extension of the stereocilia actin
496 core using short polymer annealing may allow for rapid changes in stereocilia length that are likely
497 needed to continually maintain the sensitivity of the MET machinery (Vélez-Ortega et al., 2017; Krey
498 et al., 2020).
499
500 Given the potent ability of MYO15 to nucleate actin filament polymerization *in vitro*, we infer
501 this activity must be tightly regulated in hair cells. There is extensive evidence for intramolecular
502 regulation throughout the myosin superfamily (Heissler and Sellers, 2016). For example, myosin 5
503 (MYO5A) exists in an autoinhibited conformer where the globular tail domain binds and inhibits motor
504 domain activity; binding of melanophilin (MLPH) to MYO5 releases this autoinhibition to activate the
505 motor domain (Li et al., 2005; Liu et al., 2006; Thirumurugan et al., 2006; Sato et al., 2007; Sckolnick
506 et al., 2013). Similar autoinhibitory regulation mechanisms have been described for other members of
507 the MyTH4 - FERM myosin family, *e.g.*, MYO7A and MYO10 (Umeki et al., 2009, 2011; Yang et al.,
508 2009; Sakai et al., 2011). We hypothesize that part of the elongation complex function may be to bind
509 MYO15 and shift the equilibrium between active and inhibited states. Intramolecular regulation may
510 also explain how different MYO15 isoforms independently exert their effects upon hair bundle
511 architecture (Fang et al., 2015). MYO15-1 and MYO15-2 possess an identical motor domain
512 competent to regulate actin polymerization, but differ by the addition of a 133 kDa N-terminal domain
513 (Fig. 1A). How the N-terminal domain affects the actin nucleation activity of the motor domain is an
514 important future question and will help uncover how the MYO15-1 isoform controls actin
515 polymerization in shorter stereocilia rows with active MET (Fang et al., 2015). In conclusion, we reveal
516 a new function for MYO15 and argue that defective nucleation of actin polymerization interferes with
517 stereocilia architecture and causes progressive hearing loss. We speculate that defective actin

518 nucleation by MYO15 is a central molecular pathology underlying DFNB3 hereditary hearing loss in
519 humans.
520
521 **MATERIALS AND METHODS**
522 **Mice**
523 Pedigree MPC190 was identified from a phenotype-driven mutagenesis screen undertaken at
524 the MRC Harwell Institute (Potter et al., 2016). Briefly, *N*-ethyl-*N*-nitrosourea (ENU) mutagenized
525 C57BL/6J males were mated with wild-type 'sighted C3H' (C3H.Pde6b^{+}) females. Resulting G_1 males
526 were crossed with C3H.Pde6b^{+} females to produce G_2 females, which were screened for the *Cdh23*^{ahl}
527 allele. *Cdh23*$^{+/+}$ G_2 females were backcrossed to their G_1 fathers to generate recessive G_3 pedigrees,
528 which entered a longitudinal phenotyping pipeline that included click box and ABR tests to assess
529 auditory function (Hardisty-Hughes et al., 2010). DNA from mice exhibiting hearing loss, and normal
530 hearing pedigree mates, was prepared from ear biopsies and used for linkage mapping utilizing the
531 Illumina GoldenGate Mouse Medium Density Linkage Panel (Gen-Probe Life Sciences Ltd, UK), which
532 identified a critical interval on chromosome 11. DNA was extracted from mouse MPC190/2.18a and
533 subject to whole genome sequencing employing the Illumina HiSeq platform (Oxford Genomics
534 Centre, Wellcome Trust Centre for Human Genetics). Subsequent alignment to the reference genome
535 (NCBIM38/mm10) identified a homozygous, non-synonymous coding lesion in the *Myo15* gene.
536
537 At the MRC Harwell Institute, mice were housed and maintained at the Mary Lyon Centre
538 under conditions outlined in the Home Office Code of Practice, with all animal procedures licenced by
539 the Home Office under the Animals (Scientific Procedures) Act 1986, UK and approved by the local
540 Ethical Review Committee (PBF9BD884 to MRB). At MRC Harwell, *jordan* mice were crossed to
541 C57BL/6N (*Cdh23*$^{753A>G}$) 'repaired' mice (Mianné et al., 2016) until congenic. Concurrently, *jordan*
542 mice were imported to the NIH and the University of Florida (UF) and maintained on a 'sightless C3H'
543 (C3H.Pde6b^{rd1}) background. Animal procedures were approved the Institutional Animal Care and Use
544 Committees (IACUC) at UF (#201910739 to JEB) and at the NIH (#1263-15 to TBF). Genomic DNA
545 from mouse tail biopsies was used as template in a PCR reaction with primers (5'-
546 CAGGAGGAGTACATCCGGG-3', 5'-AGACCACAGAAGTATCTGGGTCTT-3'). The resulting 161 bp
547 amplicon was analyzed by *MlsI* endonuclease digestion. Resulting restriction fragments lengths
548 unambiguously detected wild-type (161 bp) and mutant (116 bp + 45 bp) alleles.
549
550 **Auditory phenotyping + behavioral testing**

551 Auditory Brainstem Response (ABR) were recorded as previously described (Dunbar et al.,
552 2019). Briefly, mice were anaesthetised via intraperitoneal injection with ketamine hydrochloride (100
553 $mg \cdot kg^{-1}$) and xylazine (10 $mg \cdot kg^{-1}$). Anesthetized mice were placed inside a sound-attenuated
554 chamber (ETS-Lindgren) and recording electrodes (Grass Telefactor F-E2-12) placed sub dermally
555 over the vertex (active), right mastoid (reference), and left flank (ground). ABR responses were
556 collected using TDT system III hardware and BioSig software (Tucker Davis Technology). Stimuli were
557 presented free field from a ES1 transducer (TDT) calibrated at a distance of 1 cm from the right ear.
558 Stimuli consisted of 0.1 ms broadband clicks or 7 ms tone-bursts at 8 kHz, 16 kHz and 32 kHz. Each
559 stimulus was presented at a maximum 90 dB SPL, followed by decreasing steps of 5 - 10 dB SPL until
560 no replicable response peaks were observed. ABR operators were blind to genotype.
561
562 Distortion Product Oto-Acoustic Emissions (DPOAE) were recorded as a terminal procedure in
563 12 weeks old mice, as described (Dunbar et al., 2019). Mice were anaesthetised with a modified
564 ketamine/xylazine solution (see ABR), with the addition of acepromazine (2 $mg \cdot ml^{-1}$, 8% v/v).
565 Anesthetized mice had a section of the pinna removed to access the external auditory meatus. Mice
566 were placed inside a sound-attenuated chamber (ETS Lindgren), and the DPOAE probe assembly
567 was inserted into the ear canal. In-ear calibration was performed before each test. An ER10B+ low-
568 noise probe microphone (Etymotic Research) was used to measure DPOAEs near the tympanic
569 membrane. Tone stimuli were presented via separate MF1 (Tucker Davis Technology) speakers, with
570 f1 and f2 at a ratio of f2/f1 = 1.2 (L1 = 65 dB SPL, L2 = 55 dB SPL). The f1 and f2 tones were
571 presented continuously in specific tone-bursts between 8 and 32 kHz.
572
573 **Scanning electron microscopy**
574 Inner ears were dissected and fixed overnight at 4ºC in 0.1 M phosphate buffer, 2.5%
575 glutaraldehyde (Sigma-Aldrich). Post-fixed ears were decalcified in 4.3% EDTA in phosphate buffer at
576 4ºC, before dissecting out the sensory epithelium. Samples were processed with alternating 1%
577 osmium tetroxide (Agar Scientific) in 0.1 M sodium cacodylate (Sigma-Aldrich) and 1%
578 thiocarbohydrazide (Sigma-Aldrich) treatments. Osmicated samples were dehydrated in graded
579 ethanols (25% to 100%) at 4ºC and stored in 100% acetone until critical point drying with liquid CO_2
580 (EM CPD300, Leica Microsystems Ltd.). Samples were mounted onto stubs using silver paint (Agar
581 Scientific), sputter-coated with platinum (Q150R S, Quorum Technologies) and visualised with a
582 scanning electron microscope (JSM-6010LV, JEOL).
583

For morphometric analyses, image pairs from the middle cochlear turn IHC and OHC bundles were captured with a 5° tilt angle difference at a constant working distance of 20 µm. Stereocilia from at least two bundles per animal were measured using ImageJ (https://imagej.nih.gov), with a minimum of 14 stereocilia for each condition. Length measurements were taken from the rear aspect of the hair bundle, so that the length of the tallest stereocilia (row 1) could be measured from the cuticular plate insertion to the tip. Estimates for actual stereocilia length were calculated using a pseudo-eucentric tilting approach (Bariani et al., 2005). A single measure x_1 (length of stereocilium) was taken from the first image and measured again (x_2) on the corresponding 5°-tilted image pair. Perpendicular counter-measures (y_1 and y_2), matched to (x_1 and x_2) were also recorded. Equation 1 was used to estimate uncertainty (ζ) due to plane rotation. Using the uncertainty estimate ζ from Equation 1, every pair of tilted measures (x_1 and x_2) was processed using Equation 2 to obtain a close approximation (ξ) of the true length of each stereocilia measured.

$$\zeta = \frac{(\Delta y)cos\Delta\varphi + (2y_1(y_1 - \Delta y)/d)sin\Delta\varphi}{(1 + y_1(y_1 - \Delta y)/d^2 sin\Delta\varphi) + \left(\frac{\Delta y}{d}\right)\cos(2\Delta\varphi)}$$

(Equation 1)

$$\xi = \frac{2d - 2\zeta cos\Delta\varphi}{\frac{d}{x_1} + \frac{d}{x_2}}$$

(Equation 2)

Where: ζ = uncertainty estimate, ξ = estimate of true size of structure of interest, $x_{1,2}$ = tilted paired-measures of structure of interest, $y_{1,2}$ = perpendicular counter-measures to measures $x_{1,2}$, Δy = arithmetic difference of counter-measures y_1 and y_2, Δφ = tilting angle (5°), *d* = working distance (20 µm).

In addition, low-magnification (1500 - 2000X) fields of mid-turn sensory epithelium were imaged and the OHC bundles counted and visually categorised as either: 'Intact', 'Abnormal / Damaged' where the bundle had an abnormal shape or was missing stereocilia, or 'Missing Bundle' where a cuticular plate was observed with no stereocilia. Cochleae from four different animals per genotype were examined, with a total of 1344 wild type and 972 *jordan* OHC bundles.

Whole mount immunofluorescence and confocal microscopy

Mouse inner ears were fixed in 4% paraformaldehyde (EMS Diasum) in PBS for 2 hours at room temperature, washed in PBS, and then micro-dissected to isolate the cochlear sensory epithelium. Samples were permeabilized in 0.5% (v/v) Triton X-100 in PBS for 30 minutes at RT, followed by blocking in 5% normal goat serum (Sigma-Aldrich), 2% bovine serum albumin (Fraction V,

617 Roche) in PBS for 1 hour at RT. Primary antibodies were diluted in blocking solution and incubated
618 with samples at 4°C overnight. Primary IgG antibodies used were: PB48 rabbit anti-MYO15 (Liang et
619 al., 1999), HL5136 rabbit anti-WHRN (Belyantseva et al., 2005), mouse anti-EPS8 (#610143, BD
620 Biosciences), rabbit anti-GPSM2 (Ezan et al., 2013) and rabbit anti-GNAI3 (#G4040, Sigma-Aldrich).
621 After washing in PBS, samples were labelled with Alexa Fluor 488 conjugated anti-IgG secondary
622 antibodies (Life Technologies) diluted in blocking solution for 1 hour at RT. Samples were co-labelled
623 with rhodamine phalloidin (Life Technologies) and mounted with high-precision #1.5 cover glass
624 (Zeiss) using Prolong Gold (Life Technologies). Images were captured using a 63x objective (1.4 NA,
625 plan apochromat, Zeiss) and a laser scanning confocal microscope (LSM780, Zeiss).
626
627 **Actin barbed end incorporation assay**
628 Cochleae from *shaker-2* or *jordan* mice were dissected at P6 in Leibowitz L-15 media (Life
629 Technologies) and adhered to the inside surface of a petri dish lid (Greiner CellStar 35 x 10 mm). The
630 stria vascularis was left intact, as described (Xiong et al., 2014). Cochleae were cultured for 6 hours in
631 DMEM / F-12 (Life Technologies) supplemented with 1% FBS (Atlanta Biologicals) and 1.5 $\mu g \cdot mL^{-1}$
632 ampicillin at 37°C, 5% CO_2. Cochlea were incubated for 2 minutes at RT in 0.5 μM TMR-actin
633 (Cytoskeleton) diluted in labelling buffer (concentrations in mM): HEPES (20), KCl (138), EGTA (3),
634 $MgCl_2$ (4), ATP (1), DTT (0.5), 1% (w/v) bovine serum albumin (BSA), 0.2 $mg \cdot mL^{-1}$ saponin, pH 7.5.
635 Cochleae were immediately fixed for 30 mins at RT in 4% paraformaldehyde (EMS Diasum) diluted in
636 PHEM buffer (concentrations in mM): PIPES (60), HEPES (25), EGTA (10), $MgCl_2$ (2), sucrose (120),
637 pH 7.0. Fixed cochleae were permeabilized in 0.5% (v/v) Triton X-100 in PBS for 30 minutes at RT,
638 labelled with Alexa 488 phalloidin (Life Technologies), and mounted using a high-precision #1.5 cover
639 glass (Zeiss) with Prolong Gold (Life Technologies). Confocal microscopy images were captured as
640 described above.
641
642 **Expression of EGFP-MYO15-2 in mammalian cells**
643 The pEGFP-C2-Myo15-2 and pEGFP-C2-Myo15-2(sh2) plasmids expressing an N-terminal
644 EGFP fusion with the mouse MYO15 isoform 2 coding sequence (NP_874357.2) were previously
645 reported (Belyantseva et al., 2003). The pEGFP-C2-Myo15-2(jd) plasmid was generated using site
646 directed mutagenesis (QuikChange II, Agilent) to introduce the jordan (c.4940A>G) non-synonymous
647 substitution. All expression plasmids were verified by Sanger sequencing and prepared as endotoxin-
648 free, transfection grade DNA (NucleoBond Xtra Maxi EF, TakaraBio). HeLa cells (#CCL2) were
649 obtained as an authenticated, low passage stock from the American Type Culture Collection (ATCC).
650 LLC-PK1-CL4 (CL4) cells were a kind gift from Dr. James Bartles at Northwestern University. HeLa

651 and CL4 cells were cultured in high-glucose DMEM (#11995, Life Technologies), supplemented with
652 1x GlutaMAX (Life Technologies) and 10% FBS (Atlanta Biologicals), and maintained at 37°C, 5%
653 CO_2. Transfection of HeLa cells or CL4 cells was performed using Lipofectamine 3000 (Life
654 Technologies) according to the manufacturer's protocol. pEGFP-C2 (Clontech) was used as an empty
655 vector control. Cells were plated onto fibronectin (10 $\mu g \cdot mL^{-1}$) coated glass bottom culture dishes
656 (#1.5, MatTek Corp) and allowed to adhere, and in the case of CL4 cells, characteristic island
657 formation could be observed. Cells were fixed in 4% paraformaldehyde and 2% sucrose in PBS for 10
658 mins (EMS Diasum). Fixed cells were permeabilized/blocked in 0.2% (v/v) Triton X-100, 10% (v/v)
659 normal goat serum (NGS) in PBS for 1 hr at RT, followed by labelling with rhodamine phalloidin (Life
660 Technologies) and Hoechst 33342 (Life Technologies) in blocking buffer (2% NGS in PBS). Confocal
661 microscopy images were captured as described above.
662
663 **Actin purification and labelling**
664 Actin was extracted from rabbit skeletal acetone powder (Pel-Freeze, AZ) in chilled G-buffer
665 (concentrations in mM), Tris-HCl (2), ATP (0.2), $CaCl_2$ (0.1), NaN_3 (1), DTT (1), pH 8, using
666 established protocols (Spudich and Watt, 1971). Actin was additionally labelled on Cys 374 using
667 either N-(1-pyrene)-iodoacetamide (Life Technologies), or tetramethylrhodamine-5-maleimide
668 (Adipogen Life Sciences)(Criddle et al., 1985; Fujiwara et al., 2002). F-actin used for steady-state
669 ATPase and gliding filaments assays was purified through two rounds of polymerization and
670 depolymerization using ultracentrifugation. F-actin was dialyzed extensively against MOPS (4), $MgCl_2$
671 (1), EGTA (0.1), DTT (1), NaN_3 (1), pH 7.0, and its concentration measured at 290 nm (ε = 26,600 M^{-}
672 $^{1} \cdot cm^{-1}$) prior to use. Unlabelled, pyrene- and TMR-labelled G-actin for polymerization studies were
673 further purified by size exclusion chromatography (Superdex 200, Cytiva) using isocratic elution in G-
674 buffer. Fractions were exclusively taken from the falling edge of the chromatogram, to ensure the
675 recovery of monomeric actin. Concentrations and dye-labelling efficiency was determined at 290 nm
676 (actin: ε = 26,600 $M^{-1} \cdot cm^{-1}$), 344 nm (pyrene: ε = 22,000 $M^{-1} \cdot cm^{-1}$) and 550 nm (rhodamine: ε = 96,900
677 $M^{-1} \cdot cm^{-1}$). Correction factors were applied for pyrene actin, $A_{corr} = A_{290} - (0.127 * A_{344})$, and separately
678 for rhodamine actin, $A_{corr} = A_{290} - (0.208 * A_{550})$(Fujiwara et al., 2002). Biotinylated skeletal muscle
679 actin (#8109-01, HyperMol, Germany) was rehydrated, dialyzed against G-buffer and cleared by
680 ultracentrifugation for 60 minutes at 100k x *g* prior to use. For actin polymerization experiments
681 performed without free ATP in solution, G-actin stocks (with 0.2 mM ATP) were desalted (PD
682 SpinTrap G-25, Cytiva) into a modified G-buffer (no ATP): Tris-HCl (2), $CaCl_2$ (0.1), NaN_3 (1), DTT (1),
683 pH 8, immediately prior to use. Desalted G-actin (ATP) monomers were stored on ice and used within
684 3 hours.

685

686 **Expression of MYO15 and deafness mutants in *Sf*9 cells using baculovirus**

687 The baculoviral transfer vector pFastbac1 M15-2IQ-EGFP-FLAG, encoding the wild-type
688 mouse MYO15 motor domain (NP_874357.2, aa. 1 - 743) as a C-terminal fusion with EGFP and
689 FLAG moieties, was previously described (Bird et al., 2014). The expressed protein was 114 kDa. The
690 *jordan* and *shaker-2* non-synonymous substitutions were separately introduced into pFastbac1 M15-
691 2IQ-EGFP-FLAG by site-directed mutagenesis (QuikChange II, Agilent) and verified by Sanger
692 sequencing. Plasmid DNA encoding wild-type, *jordan* and *shaker-2* was separately transformed into
693 DH10Bac cells (Life Technologies) and recombinant bacmid DNA prepared following the
694 manufacturer's protocol. First passage (P1) recombinant baculovirus was generated by transfecting
695 *Sf*9 cells (Expression Systems) with bacmid DNA complexed using linear polyethylenimine (PEI MAX,
696 40,000 MW, Polysciences Inc., PA) at a 12:1 (PEI : DNA) molar ratio. *Sf*9 cells were maintained in
697 suspension culture with ESF-921 medium (Expression Systems) in a shaking incubator at 27°C. P1
698 baculovirus was amplified in *Sf*9 cells using low multiplicity of infection (MOI = 0.1) to generate P2
699 baculovirus for expression. Dual-promoter baculovirus expressing mouse UNC45B + HSP90AA1
700 chaperones (Bird et al., 2014), and bovine smooth muscle essential (MYL6, also referred to as
701 MLC17B / ELC) + chicken regulatory (MYL12B, also referred to as MLC20 / RLC) light chains, were
702 previously described (Pato et al., 1996). All baculoviruses were tittered using an end-point dilution
703 assay and the *Sf*9 Easy Titer cell line (Hopkins and Esposito, 2009). To express M15-2IQ, *Sf*9 cells
704 were seeded at a density of 2 x 10^6 cells·mL^{-1} in ESF-921, and infected simultaneously with three
705 baculoviruses at the following MOI: M15-2IQ (5), UNC45B / HSP90AA1 (5), ELC / RLC (5).The
706 myosin chaperones UNC45B and HSP90AA1 we co-expressed to aid folding, in addition to essential
707 (MYL6) and regulatory (MYL12B) muscle light chains to bind the LCBDs (Bird et al., 2014; Jiang et al.,
708 2021). Identical expressions were performed for the *shaker-2* and *jordan* variants. Cells were
709 harvested at 48 - 72 hours post-infection by centrifugation at 500 x *g* and flash frozen in liquid
710 nitrogen.

711

712 **Purification of the MYO15 motor domain**

713 M15-2IQ (wild-type, *jordan*, *shaker-2*) motor domains were purified from frozen *Sf*9 cells
714 following established protocols (Bird et al., 2014; Jiang et al., 2021). Cell pellets were lysed using a
715 Dounce homogenizer in extraction buffer (concentrations in mM): MOPS (10), NaCl (500), EGTA (1),
716 $MgCl_2$(10), ATP (2), PMSF (0.2), DTT (0.1), NaN_3 (1), leupeptin (2 μg·mL^{-1}), protease inhibitor cocktail
717 (Halt EDTA-free; Thermo Scientific), pH 7.2. Cell lysates were cleared for 30 mins at 48k x *g* and the
718 supernatant incubated with FLAG M2 affinity resin (Sigma-Aldrich) for 3 hours at 4°C. FLAG resin was

719 packed into a gravity flow column and washed with a high-salt buffer, MOPS (10), NaCl (500), EGTA
720 (1), $MgCl_2$(5), ATP (1), PMSF (0.1), DTT (0.1), NaN_3 (1), leupeptin (2 μg·mL^{-1}), pH 7.2, followed by a
721 low-salt buffer, MOPS (10), NaCl (60), EGTA (1), PMSF (0.1), DTT (0.1), NaN_3 (1), leupeptin (2
722 μg·mL^{-1}), pH 7.0. M15-2IQ protein was eluted using low-salt buffer supplemented with 0.2 mg·mL^{-1} 3x
723 FLAG peptide (American Peptide, CA). For assessment of hydrodynamic radius, purified motor
724 domains (wild-type, *jordan*, *shaker-2*) were concentrated by centrifugation (10'000 MWCO; Amicon,
725 EMD-Millipore) and directly analyzed using size exclusion chromatography (see below), alongside
726 protein size standards (Thyroglobulin (1), Ferritin (2), Aldolase (3), Conalbumin (4), Ovalbumin (5),
727 Carbonic anhydrase (6), Ribonuclease A (7); HMW + LMW gel filtration calibration kit (Cytiva). For
728 preparative scale protein production, FLAG-eluted motor domains (wild-type + *jordan*) were bound to a
729 strong anion exchanger (5/50 MonoQ GL; Cytiva) using a Purifier 10 chromatography system (GE
730 Healthcare). The column was washed with MOPS (10), NaCl (100), EGTA (1), PMSF (0.1), DTT (1),
731 pH 7.0, and a 160 CV gradient elution performed to 1M NaCl (100% B). Fractions eluting at ~31
732 mS·cm^{-1} were concentrated (10,000 MWCO) and further purified using size exclusion
733 chromatography (Superdex 200, Cytiva) with isocratic elution in MOPS (10), KCl (100), EGTA (0.1),
734 NaN_3 (1), PMSF (0.1), DTT (1), leupeptin (1 μg·mL^{-1}), pH 7.0. The M15-2IQ : ELC : RLC complex
735 (1:1:1) eluted as a single peak and was concentrated (10,000 MWCO) before determining complex
736 concentration at 280 nm (ε = 88,020 M^{-1}·cm^{-1}).
737
738 **ATPase assays**
739 Steady-state actin activated ATPase assays were measured using a NADH-coupled assay, as
740 previously reported (Bird et al., 2014). Briefly, wild-type M15-2IQ (30 nM) or *jordan* (150 nM) protein
741 was assayed in the following reaction buffer (concentration in mM): MOPS (10), KCl (50), $MgCl_2$ (5),
742 EGTA (0.1), MgATP (2), 40 U·mL^{-1} lactate dehydrogenase (Sigma-Aldrich), 200 U·mL^{-1} pyruvate
743 kinase (Sigma-Aldrich), phosphoenolpyruvate (1) (Sigma-Aldrich), NADH (0.2), pH 7.0 at 20° ± 0.1 ºC.
744 Due to its lower activity, a higher concentration (150 nM) of M15-2IQ *jordan* protein was used. The
745 concentration of F-actin in the reaction was titrated from 0 to 100 μM. The absorbance of NADH (ε =
746 6,220 M^{-1}·cm^{-1}) at 340 nm was measured using a dual-beam spectrophotometer (UV-1800, Shimadzu)
747 and the ATP hydrolysis rate calculated from the change in absorbance over time. Hydrolysis rates
748 were corrected for basal M15-2IQ ATPase activity in the absence of F-actin, and also for the ATPase
749 activity of F-actin. ATP hydrolysis rates were fit to the Michaelis-Menten equation to estimate k_{cat} and
750 k_{ATPase} using Prism (GraphPad).
751
752 **Gliding filament motility assay**

753 Motility chambers were assembled by coating a clean cover glass (#1.5) with 0.1%
754 nitrocellulose in amyl acetate (Ladd Research Industries), and attaching it to a microscope slide with
755 two strips of double-sided adhesive tape (Scotch, 3M) to form a channel approximately 3 mm wide.
756 The chamber was incubated for 5 mins in 0.1 mg·mL^{-1} anti-GFP (clone GFP-20, Sigma-Aldrich)
757 diluted with motility buffer (MB) (concentrations in mM): MOPS (20), KCl (10), $MgCl_2$ (5), EGTA (0.1),
758 pH 7.0. The surface was blocked using 1 mg·mL^{-1} BSA (Sigma-Aldrich) diluted in MB and incubated
759 for 1 min. After washing the chamber with MB, 1 μM M15-2IQ (wild-type or *jordan*) diluted in MB was
760 incubated for 1 min to functionalize the anti-GFP coated surface. The chamber was washed with 1
761 mg·mL^{-1} BSA in MB, followed by MB alone. Finally, the chamber was incubated for 2 mins with TMR-
762 phalloidin stabilized actin filaments (5 nM) diluted in MB, and subsequently washed in MB. Filaments
763 were visualized using an inverted epifluorescence microscope (Olympus IX-51) and motility recorded
764 in MB supplemented with 50 mM DTT, 2 mM ATP, 3 mM glucose, 100 μg·mL glucose oxidase, and 20
765 μg·mL catalase at 30 ± 0.5 °C. Actin filament velocities were analyzed as described (Sellers et al.,
766 1993).
767
768 **Polymerization assay**
769 Actin polymerization was measured using G-actin labelled on Cys 374 with N-(1-pyrene)-
770 iodoacetamide (see above), and a cuvette-based fluorometer (PTI Quantamaster 400, HORIBA
771 Scientific) used to excite pyrene at 365 nm and capture fluorescence emission at 407 nm. Gel filtered
772 G-actin (10% pyrene labelled, with free ATP, or desalted) was converted to the physiological Mg^{2+}
773 bound form by addition of 50 μM $MgCl_2$ and 0.2 mM EGTA for exactly two minutes at room
774 temperature. The polymerization reaction was initiated by mixing G-actin (3 x stock) with KMEI buffer
775 (1.5x stock) in a 1:2 ratio, respectively. Myosin (wild-type or *jordan*) was included in the 1.5x KMEI
776 buffer as needed. Final concentrations were 2 μM G-actin and 1 μM myosin, in assay buffer
777 (concentrations in mM): KCl (50), $MgCl_2$ (1), EGTA (1), imidazole (10), pH 7.0 at 25° ± 0.1 ºC. Data
778 were corrected for dead-time and fluorescence recorded until the transient reached plateau, or for a
779 maximum of 3 hours. Fluorescence derivatives with respect to time were processed in Prism
780 (GraphPad). Half times were calculated as described (Hansen et al., 2013).
781
782 **TIRF single-filament polymerization assay**
783 High-tolerance cover slips (24 × 50 mm, #1.5, Marienfeld Superior, Germany) were cleaned by
784 sequential sonication (10 mins each) in 2% Hellmanex III (Hellma, Germany), 1M KOH, 100% ethanol,
785 and finally Milli-Q water. Cover slips were dried under a nitrogen stream and processed for 10 mins
786 under argon plasma (ZEPTO, Diener Electronic, Germany). A mixture of mPEG-silane (2 mg·mL^{-1},

787 Laysan Bio, AL) and biotin–PEG–silane (2 μg·mL^{-1}, Laysan Bio) was prepared in 96% ethanol, 0.1%
788 (v/v) HCl. Cover slips were coated with 100 μL of the mPEG mixture and baked at 70°C for 1 hour.
789 Cover slips were rinsed twice in 96% ethanol, sonicated for 10 mins, followed by two rinses in Milli-Q,
790 sonicated for 10 mins in Milli-Q, and finally dried under a nitrogen stream. Flow chambers were
791 assembled using double-sided sticky tape to create a 3 mm wide channel on a glass slide.
792 Functionalized coverslips were placed over the tape and firmly pushed down to seal the flow chamber.
793 Immediately prior to use, flow cells were washed with buffer T50 (concentrations in mM): Tris·HCl
794 (10), KCl (50), DTT (1), pH 8.0. Flow cells were sequentially washed with 0.1 mg·mL^{-1} (Neutravidin,
795 Thermo Scientific) in T50 for 1 min, followed by a wash with 1 mg·mL^{-1} bovine serum albumin (A0281,
796 Sigma Aldrich) in T50 for 30 s, and a final wash of T50. Experiments were performed in the following
797 reaction buffer (final concentration in mM): KCl (50), $MgCl_2$ (1), EGTA (1), imidazole (10), ATP (0.025),
798 DTT (10), glucose (15), 0.5% methylcellulose, 20 μg·mL catalase, 100 μg·mL glucose oxidase, pH 7.0.
799 G-actin (1 μM total) was included in the reaction with TMR-actin (20%) and biotin-actin (10%) doping.
800 Purified myosin motor domain (1 μM) was optionally added, as needed. The reaction was loaded into
801 the flow cell and immediately mounted onto an inverted microscope (Nikon Ti-E2) equipped with an oil
802 immersion objective (CFI Apochromat TIRF 100x, 1.49 N.A., Nikon) for objective-style total internal
803 reflection fluorescence (TIRF) microscopy (H-TIRF, Nikon). The flow cell was illuminated using a 561
804 nm laser line, and emission filtered using a bandpass filter (ET630/75m, Chroma). Time-lapse images
805 were captured on an EM-CCD camera (iXon Ultra 888, Andor) controlled by NIS-Elements (AR
806 version 5.2, Nikon). Samples were imaged at 21 ± 1°C. The assay dead-time was typically 45 - 60 s,
807 and was included in data analyses.
808
809 Images were pre-processed in FIJI (https://fiji.sc)(Schindelin et al., 2012) by performing
810 background subtraction and image registration (descriptor-based series registration, 2d/3d +t). Actin
811 filament densities were quantified using the Analyze Particle command (size > 3 pixel^2, circularity: 0.0-
812 1.0) to count discrete particles within a 50 x 50 μm region of interest (ROI) that was randomly selected
813 from the field of view. A minimum of 3 experiments, from two independent protein preparations, were
814 analyzed for each condition. Filament elongation rates were calculated from time-lapse TIRF imaging
815 sequences using kymographs generated in Elements Software (version 5.2, Nikon). At least 40
816 filaments from two independent experiments were analyzed for each condition.
817
818 **Statistical analyses**
819 All statistical calculations and non-linear regressions were performed in Prism (GraphPad).

820 Regression fit parameters are quoted as mean ± SEM, and data points as mean ± SD, unless
821 otherwise stated. Statistical significance: * $p < 0.05$, ** $p < 0.01$, *** $p < 0.001$, **** $p < 0.0001$.
822
823 **AUTHOR CONTRIBUTIONS**

824 Conceptualization:	JEB, MRB
825 Investigation:	ZGM, FJ, CA, MB, CFA, AS, JW, RH, DCS, SMC, AP, SM, EW,
826	YT, MRB, JEB
827 Formal analysis:	ZGM, FJ, CA, MB, RG, AS, CFA, JW, RH, DCS, SMC, AP, SM,
828	EW, YT, JRS, SDMB, GMA TBF, MRB, JEB
829 Writing - original draft:	ZGM, FJ, CA, MB, MRB, JEB
830 Writing – review and editing:	All authors.
831 Project administration:	JEB
832 Funding acquisition:	JRS, SDMB, TBF, MRB, JEB

833
834 **ACKNOWLEDGEMENTS**
835 We thank Mireille Montcouquiol for the gift of GPSM2 antisera, James Bartles for the gift of
836 LLC-PK1-CL4 cells, Tracy Fitzgerald at the NIDCD Mouse Auditory Testing Core for expert technical
837 assistance, W. Clay Smith for use of fluorometry equipment, Peter Höök, H. Lee Sweeney and Tom
838 Pollard for insightful discussions, and Peter Barr-Gillespie for critical feedback on the manuscript. This
839 research was supported (in part) by the Intramural Research Program of the NIH (NIDCD DC000039
840 to TBF, NHLBI HL006049 to JRS), the Medical Research Council (MC_U142684175 to SDMB,
841 MC_UP_1503/2 to MRB) and National Institute on Deafness and Other Communication Disorders of
842 the National Institutes of Health under Award Number R01DC018827 (to JEB). The content is solely
843 the responsibility of the authors and does not necessarily represent the official views of the National
844 Institutes of Health. The funding bodies had no role in study design, data collection or analysis,
845 decision to publish, or preparation of the manuscript.
846
847 **ACKNOWLEDGEMENTS**
848 The authors declare that no competing interests exist.
849
850 **REFERENCES**
851 Ahuja R, Pinyol R, Reichenbach N, Custer L, Klingensmith J, Kessels MM, Qualmann B (2007)
852 Cordon-bleu is an actin nucleation factor and controls neuronal morphology. Cell 131:337–350.

853 Anderson DW, Probst FJ, Belyantseva IA, Fridell RA, Beyer L, Martin DM, Wu D, Kachar B, Friedman
854 TB, Raphael Y, Camper SA (2000) The motor and tail regions of myosin XV are critical for normal
855 structure and function of auditory and vestibular hair cells. Hum Mol Genet 9:1729–1738.

856 Avenarius MR, Krey JF, Dumont RA, Morgan CP, Benson CB, Vijayakumar S, Cunningham CL,
857 Scheffer DI, Corey DP, Müller U, Jones SM, Barr-Gillespie PG (2017) Heterodimeric capping protein
858 is required for stereocilia length and width regulation. J Cell Biol 216:3861–3881.

859 Avraham KB, Hasson T, Steel KP, Kingsley DM, Russell LB, Mooseker MS, Copeland NG, Jenkins
860 NA (1995) The mouse Snell's waltzer deafness gene encodes an unconventional myosin required for
861 structural integrity of inner ear hair cells. Nat Genet 11:369–375.

862 Bariani P, De Chiffre L, Hansen HN, Horsewell A (2005) Investigation on the traceability of three
863 dimensional scanning electron microscope measurements based on the stereo-pair technique. Precis
864 Eng 29:219–228.

865 Barr-Gillespie P-G (2015) Assembly of hair bundles, an amazing problem for cell biology. Mol Biol Cell
866 26:2727–2732.

867 Belyantseva IA, Boger ET, Friedman TB (2003) Myosin XVa localizes to the tips of inner ear sensory
868 cell stereocilia and is essential for staircase formation of the hair bundle. Proc Natl Acad Sci U S A
869 100:13958–13963.

870 Belyantseva IA, Boger ET, Naz S, Frolenkov GI, Sellers JR, Ahmed ZM, Griffith AJ, Friedman TB
871 (2005) Myosin-XVa is required for tip localization of whirlin and differential elongation of hair-cell
872 stereocilia. Nat Cell Biol 7:148–156.

873 Beurg M, Fettiplace R, Nam J-H, Ricci AJ (2009) Localization of inner hair cell mechanotransducer
874 channels using high-speed calcium imaging. Nat Neurosci 12:553–558.

875 Bird JE, Barzik M, Drummond MC, Sutton DC, Goodman SM, Morozko EL, Cole SM, Boukhvalova
876 AK, Skidmore J, Syam D, Wilson EA, Fitzgerald T, Rehman AU, Martin DM, Boger ET, Belyantseva
877 IA, Friedman TB (2017) Harnessing molecular motors for nanoscale pulldown in live cells. Mol Biol
878 Cell 28:463–475.

879 Bird JE, Takagi Y, Billington N, Strub M-P, Sellers JR, Friedman TB (2014) Chaperone-enhanced
880 purification of unconventional myosin 15, a molecular motor specialized for stereocilia protein
881 trafficking. Proc Natl Acad Sci U S A 111:12390–12395.

882 Brawley CM, Rock RS (2009) Unconventional myosin traffic in cells reveals a selective actin
883 cytoskeleton. Proc Natl Acad Sci U S A 106:9685–9690.

884 Cooper JA, Walker SB, Pollard TD (1983) Pyrene actin: documentation of the validity of a sensitive
885 assay for actin polymerization. J Muscle Res Cell Motil 4:253–262.

886 Criddle AH, Geeves MA, Jeffries T (1985) The use of actin labelled with N-(1-pyrenyl)iodoacetamide
887 to study the interaction of actin with myosin subfragments and troponin/tropomyosin. Biochem J
888 232:343–349.

889 Delprat B, Michel V, Goodyear R, Yamasaki Y, Michalski N, El-Amraoui A, Perfettini I, Legrain P,
890 Richardson G, Hardelin J-P, Petit C (2005) Myosin XVa and whirlin, two deafness gene products

891 required for hair bundle growth, are located at the stereocilia tips and interact directly. Hum Mol Genet
892 14:401–410.

893 Dominguez R, Holmes KC (2011) Actin structure and function. Annu Rev Biophys 40:169–186.

894 Drummond MC, Barzik M, Bird JE, Zhang D-S, Lechene CP, Corey DP, Cunningham LL, Friedman
895 TB (2015) Live-cell imaging of actin dynamics reveals mechanisms of stereocilia length regulation in
896 the inner ear. Nat Commun 6:6873.

897 Dunbar LA et al. (2019) Clarin-2 is essential for hearing by maintaining stereocilia integrity and
898 function. EMBO Mol Med 11:e10288.

899 Ebrahim S, Avenarius MR, Grati M, Krey JF, Windsor AM, Sousa AD, Ballesteros A, Cui R, Millis BA,
900 Salles FT, Baird MA, Davidson MW, Jones SM, Choi D, Dong L, Raval MH, Yengo CM, Barr-Gillespie
901 PG, Kachar B (2016) Stereocilia-staircase spacing is influenced by myosin III motors and their cargos
902 espin-1 and espin-like. Nat Commun 7:10833.

903 Ezan J, Lasvaux L, Gezer A, Novakovic A, May-Simera H, Belotti E, Lhoumeau A-C, Birnbaumer L,
904 Beer-Hammer S, Borg J-P, Le Bivic A, Nürnberg B, Sans N, Montcouquiol M (2013) Primary cilium
905 migration depends on G-protein signalling control of subapical cytoskeleton. Nat Cell Biol 15:1107–
906 1115.

907 Fang Q, Indzhykulian AA, Mustapha M, Riordan GP, Dolan DF, Friedman TB, Belyantseva IA,
908 Frolenkov GI, Camper SA, Bird JE (2015) The 133-kDa N-terminal domain enables myosin 15 to
909 maintain mechanotransducing stereocilia and is essential for hearing. eLife 4.

910 Fievez S, Carlier MF (1993) Conformational changes in subdomain-2 of G-actin upon polymerization
911 into F-actin and upon binding myosin subfragment-1. FEBS Lett 316:186–190.

912 Fievez S, Carlier MF, Pantaloni D (1997a) Mechanism of myosin subfragment-1-induced assembly of
913 CaG-actin and MgG-actin into F-actin-S1-decorated filaments. Biochemistry 36:11843–11850.

914 Fievez S, Pantaloni D, Carlier MF (1997b) Kinetics of myosin subfragment-1-induced condensation of
915 G-actin into oligomers, precursors in the assembly of F-actin-S1. Role of the tightly bound metal ion
916 and ATP hydrolysis. Biochemistry 36:11837–11842.

917 Flock A, Cheung HC (1977) Actin filaments in sensory hairs of inner ear receptor cells. J Cell Biol
918 75:339–343.

919 Friedman TB, Liang Y, Weber JL, Hinnant JT, Barber TD, Winata S, Arhya IN, Asher JH (1995) A
920 gene for congenital, recessive deafness DFNB3 maps to the pericentromeric region of chromosome
921 17. Nat Genet 9:86–91.

922 Fujiwara I, Takahashi S, Tadakuma H, Funatsu T, Ishiwata S (2002) Microscopic analysis of
923 polymerization dynamics with individual actin filaments. Nat Cell Biol 4:666–673.

924 Gibson F, Walsh J, Mburu P, Varela A, Brown KA, Antonio M, Beisel KW, Steel KP, Brown SD (1995)
925 A type VII myosin encoded by the mouse deafness gene shaker-1. Nature 374:62–64.

926 Gillespie PG, Corey DP (1997) Myosin and adaptation by hair cells. Neuron 19:955–958.

927 Gong R, Jiang F, Moreland ZG, Reynolds M, Espinosa de los Reyes S, Gurel PS, Shams A, Bowl MR,
928 Bird JE, Alushin GM (2021) Structural basis for tunable control of actin dynamics by myosin-15 in
929 mechanosensory stereocilia. bioRxiv 2021.07.09.451843.

930 Hansen SD, Zuchero JB, Mullins RD (2013) Cytoplasmic actin: purification and single molecule
931 assembly assays. Methods Mol Biol Clifton NJ 1046:145–170.

932 Hardisty-Hughes RE, Parker A, Brown SDM (2010) A hearing and vestibular phenotyping pipeline to
933 identify mouse mutants with hearing impairment. Nat Protoc 5:177–190.

934 Hartman MA, Spudich JA (2012) The myosin superfamily at a glance. J Cell Sci 125:1627–1632.

935 Hasson T, Gillespie PG, Garcia JA, MacDonald RB, Zhao Y, Yee AG, Mooseker MS, Corey DP (1997)
936 Unconventional myosins in inner-ear sensory epithelia. J Cell Biol 137:1287–1307.

937 Heissler SM, Sellers JR (2016) Various Themes of Myosin Regulation. J Mol Biol 428:1927–1946.

938 Holt JR, Gillespie SKH, Provance DW, Shah K, Shokat KM, Corey DP, Mercer JA, Gillespie PG
939 (2002) A chemical-genetic strategy implicates myosin-1c in adaptation by hair cells. Cell 108:371–381.

940 Hopkins R, Esposito D (2009) A rapid method for titrating baculovirus stocks using the Sf-9 Easy Titer
941 cell line. BioTechniques 47:785–788.

942 Houdusse A, Sweeney HL (2016) How Myosin Generates Force on Actin Filaments. Trends Biochem
943 Sci 41:989–997.

944 Jiang F, Takagi Y, Shams A, Heissler SM, Friedman TB, Sellers JR, Bird JE (2021) The ATPase
945 mechanism of myosin 15, the molecular motor mutated in DFNB3 human deafness. J Biol Chem
946 296:100243.

947 Kaltenbach JA, Falzarano PR, Simpson TH (1994) Postnatal development of the hamster cochlea. II.
948 Growth and differentiation of stereocilia bundles. J Comp Neurol 350:187–198.

949 Kerber ML, Jacobs DT, Campagnola L, Dunn BD, Yin T, Sousa AD, Quintero OA, Cheney RE (2009)
950 A novel form of motility in filopodia revealed by imaging myosin-X at the single-molecule level. Curr
951 Biol CB 19:967–973.

952 Kinosian HJ, Selden LA, Estes JE, Gershman LC (1993) Actin filament annealing in the presence of
953 ATP and phalloidin. Biochemistry 32:12353–12357.

954 Krey JF, Barr-Gillespie PG (2019) Molecular Composition of Vestibular Hair Bundles. Cold Spring
955 Harb Perspect Med 9:a033209.

956 Krey JF, Chatterjee P, Dumont RA, O'Sullivan M, Choi D, Bird JE, Barr-Gillespie PG (2020)
957 Mechanotransduction-Dependent Control of Stereocilia Dimensions and Row Identity in Inner Hair
958 Cells. Curr Biol CB 30:442-454.e7.

959 Kuhn JR, Pollard TD (2005) Real-time measurements of actin filament polymerization by total internal
960 reflection fluorescence microscopy. Biophys J 88:1387–1402.

961 Lheureux K, Forné T, Chaussepied P (1993) Interaction and polymerization of the G-actin-myosin
962 head complex: effect of DNase I. Biochemistry 32:10005–10014.

963 Li X-D, Ikebe R, Ikebe M (2005) Activation of myosin Va function by melanophilin, a specific docking
964 partner of myosin Va. J Biol Chem 280:17815–17822.

965 Liang Y, Wang A, Belyantseva IA, Anderson DW, Probst FJ, Barber TD, Miller W, Touchman JW, Jin
966 L, Sullivan SL, Sellers JR, Camper SA, Lloyd RV, Kachar B, Friedman TB, Fridell RA (1999)
967 Characterization of the human and mouse unconventional myosin XV genes responsible for hereditary
968 deafness DFNB3 and shaker 2. Genomics 61:243–258.

969 Liu J, Taylor DW, Krementsova EB, Trybus KM, Taylor KA (2006) Three-dimensional structure of the
970 myosin V inhibited state by cryoelectron tomography. Nature 442:208–211.

971 Machesky LM, Atkinson SJ, Ampe C, Vandekerckhove J, Pollard TD (1994) Purification of a cortical
972 complex containing two unconventional actins from Acanthamoeba by affinity chromatography on
973 profilin-agarose. J Cell Biol 127:107–115.

974 Manor U, Disanza A, Grati M, Andrade L, Lin H, Di Fiore PP, Scita G, Kachar B (2011) Regulation of
975 stereocilia length by myosin XVa and whirlin depends on the actin-regulatory protein Eps8. Curr Biol
976 CB 21:167–172.

977 Mauriac SA, Hien YE, Bird JE, Carvalho SD-S, Peyroutou R, Lee SC, Moreau MM, Blanc J-M, Geyser
978 A, Medina C, Thoumine O, Beer-Hammer S, Friedman TB, Rüttiger L, Forge A, Nürnberg B, Sans N,
979 Montcouquiol M (2017) Defective Gpsm2/Gαi3 signalling disrupts stereocilia development and growth
980 cone actin dynamics in Chudley-McCullough syndrome. Nat Commun 8:14907.

981 Mburu P et al. (2003) Defects in whirlin, a PDZ domain molecule involved in stereocilia elongation,
982 cause deafness in the whirler mouse and families with DFNB31. Nat Genet 34:421–428.

983 Mianné J, Chessum L, Kumar S, Aguilar C, Codner G, Hutchison M, Parker A, Mallon A-M, Wells S,
984 Simon MM, Teboul L, Brown SDM, Bowl MR (2016) Correction of the auditory phenotype in C57BL/6N
985 mice via CRISPR/Cas9-mediated homology directed repair. Genome Med 8:16.

986 Miller L, Phillips M, Reisler E (1988) Polymerization of G-actin by myosin subfragment 1. J Biol Chem
987 263:1996–2002.

988 Mullins RD, Heuser JA, Pollard TD (1998) The interaction of Arp2/3 complex with actin: nucleation,
989 high affinity pointed end capping, and formation of branching networks of filaments. Proc Natl Acad
990 Sci U S A 95:6181–6186.

991 Mullins RD, Stafford WF, Pollard TD (1997) Structure, subunit topology, and actin-binding activity of
992 the Arp2/3 complex from Acanthamoeba. J Cell Biol 136:331–343.

993 Murphy DB, Gray RO, Grasser WA, Pollard TD (1988) Direct demonstration of actin filament
994 annealing in vitro. J Cell Biol 106:1947–1954.

995 Nagy S, Ricca BL, Norstrom MF, Courson DS, Brawley CM, Smithback PA, Rock RS (2008) A myosin
996 motor that selects bundled actin for motility. Proc Natl Acad Sci U S A 105:9616–9620.

997 Narayanan P, Chatterton P, Ikeda A, Ikeda S, Corey DP, Ervasti JM, Perrin BJ (2015) Length
998 regulation of mechanosensitive stereocilia depends on very slow actin dynamics and filament-severing
999 proteins. Nat Commun 6:6855.

000 Okreglak V, Drubin DG (2010) Loss of Aip1 reveals a role in maintaining the actin monomer pool and
001 an in vivo oligomer assembly pathway. J Cell Biol 188:769–777.

002 Pato MD, Sellers JR, Preston YA, Harvey EV, Adelstein RS (1996) Baculovirus expression of chicken
003 nonmuscle heavy meromyosin II-B. Characterization of alternatively spliced isoforms. J Biol Chem
004 271:2689–2695.

005 Peng AW, Belyantseva IA, Hsu PD, Friedman TB, Heller S (2009) Twinfilin 2 regulates actin filament
006 lengths in cochlear stereocilia. J Neurosci Off J Soc Neurosci 29:15083–15088.

007 Potter PK et al. (2016) Novel gene function revealed by mouse mutagenesis screens for models of
008 age-related disease. Nat Commun 7:12444.

009 Probst FJ, Fridell RA, Raphael Y, Saunders TL, Wang A, Liang Y, Morell RJ, Touchman JW, Lyons
010 RH, Noben-Trauth K, Friedman TB, Camper SA (1998) Correction of deafness in shaker-2 mice by an
011 unconventional myosin in a BAC transgene. Science 280:1444–1447.

012 Quinlan ME, Heuser JE, Kerkhoff E, Mullins RD (2005) Drosophila Spire is an actin nucleation factor.
013 Nature 433:382–388.

014 Rehman AU, Bird JE, Faridi R, Shahzad M, Shah S, Lee K, Khan SN, Imtiaz A, Ahmed ZM, Riazuddin
015 S, Santos-Cortez RLP, Ahmad W, Leal SM, Riazuddin S, Friedman TB (2016) Mutational Spectrum of
016 MYO15A and the Molecular Mechanisms of DFNB3 Human Deafness. Hum Mutat 37:991–1003.

017 Reymann A-C, Boujemaa-Paterski R, Martiel J-L, Guérin C, Cao W, Chin HF, De La Cruz EM, Théry
018 M, Blanchoin L (2012) Actin network architecture can determine myosin motor activity. Science
019 336:1310–1314.

020 Richardson GP, de Monvel JB, Petit C (2011) How the genetics of deafness illuminates auditory
021 physiology. Annu Rev Physiol 73:311–334.

022 Ropars V, Yang Z, Isabet T, Blanc F, Zhou K, Lin T, Liu X, Hissier P, Samazan F, Amigues B, Yang
023 ED, Park H, Pylypenko O, Cecchini M, Sindelar CV, Sweeney HL, Houdusse A (2016) The myosin X
024 motor is optimized for movement on actin bundles. Nat Commun 7:12456.

025 Rzadzinska AK, Schneider ME, Davies C, Riordan GP, Kachar B (2004) An actin molecular treadmill
026 and myosins maintain stereocilia functional architecture and self-renewal. J Cell Biol 164:887–897.

027 Sagot I, Rodal AA, Moseley J, Goode BL, Pellman D (2002) An actin nucleation mechanism mediated
028 by Bni1 and profilin. Nat Cell Biol 4:626–631.

029 Sakai T, Umeki N, Ikebe R, Ikebe M (2011) Cargo binding activates myosin VIIA motor function in
030 cells. Proc Natl Acad Sci U S A 108:7028–7033.

031 Salles FT, Merritt RC, Manor U, Dougherty GW, Sousa AD, Moore JE, Yengo CM, Dosé AC, Kachar
032 B (2009) Myosin IIIa boosts elongation of stereocilia by transporting espin 1 to the plus ends of actin
033 filaments. Nat Cell Biol 11:443–450.

034 Sato O, Li X-D, Ikebe M (2007) Myosin Va becomes a low duty ratio motor in the inhibited form. J Biol
035 Chem 282:13228–13239.

036 Schindelin J, Arganda-Carreras I, Frise E, Kaynig V, Longair M, Pietzsch T, Preibisch S, Rueden C,
037 Saalfeld S, Schmid B, Tinevez J-Y, White DJ, Hartenstein V, Eliceiri K, Tomancak P, Cardona A
038 (2012) Fiji: an open-source platform for biological-image analysis. Nat Methods 9:676–682.

039 Schneider ME, Belyantseva IA, Azevedo RB, Kachar B (2002) Rapid renewal of auditory hair bundles.
040 Nature 418:837–838.

041 Sckolnick M, Krementsova EB, Warshaw DM, Trybus KM (2013) More than just a cargo adapter,
042 melanophilin prolongs and slows processive runs of myosin Va. J Biol Chem 288:29313–29322.

043 Sellers JR, Cuda G, Wang F, Homsher E (1993) Myosin-specific adaptations of the motility assay.
044 Methods Cell Biol 39:23–49.

045 Sept D, Xu J, Pollard TD, McCammon JA (1999) Annealing accounts for the length of actin filaments
046 formed by spontaneous polymerization. Biophys J 77:2911–2919.

047 Shin J-B, Streijger F, Beynon A, Peters T, Gadzalla L, McMillen D, Bystrom C, Van der Zee CEEM,
048 Wallimann T, Gillespie PG (2007) Hair Bundles Are Specialized for ATP Delivery via Creatine Kinase.
049 Neuron 53:371–386.

050 Spudich JA, Watt S (1971) The regulation of rabbit skeletal muscle contraction. I. Biochemical studies
051 of the interaction of the tropomyosin-troponin complex with actin and the proteolytic fragments of
052 myosin. J Biol Chem 246:4866–4871.

053 Stepanyan R, Belyantseva IA, Griffith AJ, Friedman TB, Frolenkov GI (2006) Auditory
054 mechanotransduction in the absence of functional myosin-XVa. J Physiol 576:801–808.

055 Tadenev ALD, Akturk A, Devanney N, Mathur PD, Clark AM, Yang J, Tarchini B (2019) GPSM2-GNAI
056 Specifies the Tallest Stereocilia and Defines Hair Bundle Row Identity. Curr Biol CB 29:921-934.e4.

057 Tarchini B, Tadenev ALD, Devanney N, Cayouette M (2016) A link between planar polarity and
058 staircase-like bundle architecture in hair cells. Dev Camb Engl 143:3926–3932.

059 Thirumurugan K, Sakamoto T, Hammer JA, Sellers JR, Knight PJ (2006) The cargo-binding domain
060 regulates structure and activity of myosin 5. Nature 442:212–215.

061 Tilney LG, Cotanche DA, Tilney MS (1992) Actin filaments, stereocilia and hair cells of the bird
062 cochlea. VI. How the number and arrangement of stereocilia are determined. Dev Camb Engl
063 116:213–226.

064 Tilney LG, Derosier DJ, Mulroy MJ (1980) The organization of actin filaments in the stereocilia of
065 cochlear hair cells. J Cell Biol 86:244–259.

066 Umeki N, Jung HS, Sakai T, Sato O, Ikebe R, Ikebe M (2011) Phospholipid-dependent regulation of
067 the motor activity of myosin X. Nat Struct Mol Biol 18:783–788.

068 Umeki N, Jung HS, Watanabe S, Sakai T, Li X, Ikebe R, Craig R, Ikebe M (2009) The tail binds to the
069 head-neck domain, inhibiting ATPase activity of myosin VIIA. Proc Natl Acad Sci U S A 106:8483–
070 8488.

071 Vélez-Ortega AC, Freeman MJ, Indzhykulian AA, Grossheim JM, Frolenkov GI (2017)
072 Mechanotransduction current is essential for stability of the transducing stereocilia in mammalian
073 auditory hair cells. eLife 6.

074 Vélez-Ortega AC, Frolenkov GI (2019) Building and repairing the stereocilia cytoskeleton in
075 mammalian auditory hair cells. Hear Res 376:47–57.

076 Wang A, Liang Y, Fridell RA, Probst FJ, Wilcox ER, Touchman JW, Morton CC, Morell RJ, Noben-
077 Trauth K, Camper SA, Friedman TB (1998) Association of unconventional myosin MYO15 mutations
078 with human nonsyndromic deafness DFNB3. Science 280:1447–1451.

079 Xiong W, Wagner T, Yan L, Grillet N, Müller U (2014) Using injectoporation to deliver genes to
080 mechanosensory hair cells. Nat Protoc 9:2438–2449.

081 Yagi K, Mase R, Sakakibara I, Asai H (1965) FUNCTION OF HEAVY MEROMYOSIN IN THE
082 ACCELERATION OF ACTIN POLYMERIZATION. J Biol Chem 240:2448–2454.

083 Yang Y, Baboolal TG, Siththanandan V, Chen M, Walker ML, Knight PJ, Peckham M, Sellers JR
084 (2009) A FERM domain autoregulates Drosophila myosin 7a activity. Proc Natl Acad Sci U S A
085 106:4189–4194.

086 Young G et al. (2018) Quantitative mass imaging of single biological macromolecules. Science
087 360:423–427.

088 Zampini V, Rüttiger L, Johnson SL, Franz C, Furness DN, Waldhaus J, Xiong H, Hackney CM, Holley
089 MC, Offenhauser N, Di Fiore PP, Knipper M, Masetto S, Marcotti W (2011) Eps8 regulates hair bundle
090 length and functional maturation of mammalian auditory hair cells. PLoS Biol 9:e1001048.

091 Zhang D-S, Piazza V, Perrin BJ, Rzadzinska AK, Poczatek JC, Wang M, Prosser HM, Ervasti JM,
092 Corey DP, Lechene CP (2012) Multi-isotope imaging mass spectrometry reveals slow protein turnover
093 in hair-cell stereocilia. Nature 481:520–524.

094 Zheng L, Zheng J, Whitlon DS, García-Añoveros J, Bartles JR (2010) Targeting of the hair cell
095 proteins cadherin 23, harmonin, myosin XVa, espin, and prestin in an epithelial cell model. J Neurosci
096 Off J Soc Neurosci 30:7187–7201.

097

098

099

FIGURE LEGENDS

FIGURE 1

A) Schematic showing the protein domains of the long (MYO15-1) and short (MYO15-2) isoforms encoded by the *Myo15* gene. The *jordan* and *shaker-2* deafness mutations are shown. **B)** ABR phenotyping of the *jordan* pedigree at 3 months identified 10 mice with statistically elevated hearing thresholds (red circles) for click and at 8, 16 and 32 kHz stimuli, compared to their normal hearing pedigree mates (n = 73, black circles). Statistical outliers were detected using robust regression and outlier removal (red circles, ROUT, Q = 1%). Thresholds of affected mice that did not respond to the highest intensity stimulus (90 dB SPL) are recorded as 95 dB SPL. Data are mean ± SD. **C)** Evolutionary conservation of the aspartate (D) residue of MYO15 altered to glycine (G) in *jordan* mice that causes hearing loss. Residue positions refer to mouse MYO15-1 (NP_034992.2). **D)** ABR recordings of $Myo15^{jd/sh2}$ compound heterozygotes at P28 shows profound hearing loss, with thresholds elevated compared with normal hearing $Myo15^{+/jd}$ *or* $Myo15^{+/sh2}$ littermates. **E-F)** Longitudinal auditory phenotyping of *jordan* mice at 1- (E) and 3- (F) months of age. ABR recordings show that $Myo15^{jd/jd}$ mice (red, n=10) exhibit a progressive, moderate-to-severe hearing loss affecting all frequencies, whereas age-matched $Myo15^{+/+}$(black, n=10) and $Myo15^{+/jd}$ (grey, n=15) littermate controls have normal thresholds (15 - 45 dB SPL). $Myo15^{+/+}$ *vs* $Myo15^{jd/jd}$ comparison, ANOVA with Tukey's multiple comparisons test.

FIGURE 2

A-F) Representative SEM images of stereocilia bundles from $Myo15^{+/+}$, $Myo15^{jd/jd}$, and $Myo15^{sh2/sh2}$ OHCs (A,C,E) and IHCs (B,D,F) at P8. In $Myo15^{+/+}$ mice, both IHC and OHC bundles display the characteristic staircase architecture with 3 stereocilia ranks of increasing height. IHC and OHC bundles from either $Myo15^{jd/jd}$ and $Myo15^{sh2/sh2}$ mice are shorter in height than the wild-type bundles. $Myo15^{jd/jd}$ stereocilia taper in height towards the periphery of the bundle (white arrows). **G)** Projected heights of tallest (row 1) OHC stereocilia at P8 are 1.2 ± 0.1 µm ($Myo15^{+/+}$, 58 stereocilia from 4 mice), 0.8 ± 0.1 µm ($Myo15^{jd/jd}$, 60 stereocilia from 4 mice), and 0.4 ± 0.1 µm ($Myo15^{sh2/sh2}$, 50 stereocilia from 2 mice). **H)** Projected heights of tallest (row 1) IHC stereocilia at P8 are 2.2 ± 0.2 µm ($Myo15^{+/+}$, 47 stereocilia from 4 mice), 1.3 ± 0.1 µm ($Myo15^{jd/jd}$, 47 stereocilia from 4 mice), and 0.9 ± 0.1 µm ($Myo15^{sh2/sh2}$, 30 stereocilia from 2 mice). Brown-Forsythe and Welch ANOVA with Dunnett's T3 multiple comparisons test. Images are from mid-cochlear turn. Scale bars, 1 µm.

134 **FIGURE 3**

135 **A,B)** Immunofluorescence (IF) confocal images showing anti-MYO15 (green, PB48) in control *Myo15*$^{+/jd}$,
136 *Myo15*$^{sh2/sh2}$ and *Myo15*$^{jd/jd}$ IHCs fixed at P14 (A), or P7 (B). Phalloidin was used to label F-actin
137 (magenta). **C)** IF confocal images of elongation complex proteins (green) in control *Myo15*$^{+/jd}$ and
138 *Myo15*$^{jd/jd}$ IHCs fixed at P7, overlaid with phalloidin labelled F-actin (magenta). Images are
139 representative of data from at least two independent animals per genotype / antibody, and are shown
140 as maximum intensity projections reconstructed from z-stacks. Scale bars, 10 µm.

141

142 **FIGURE 4**

143 **A)** Actin barbed-end assay in detergent-permeabilized hair cells from mouse cochlear explant cultures
144 at P6. TMR-labelled G-actin (green) was added prior to fixation to identify uncapped barbed ends.
145 Phalloidin labelling of F-actin (magenta) is overlaid. In both *Myo15*$^{jd/jd}$ and littermate *Myo15*$^{+/jd}$ controls,
146 barbed-ends were detected at row 2 stereocilia tips, and at the tips of all stereocilia rows in *Myo15*$^{sh2/sh2}$
147 hair cells. **B)** HeLa cells were transfected with EGFP-tagged *Myo15-2* expression constructs or EGFP
148 alone (green) as indicated, fixed and probed with phalloidin (magenta) and Hoechst (blue). EGFP-M15
149 (wt) trafficked to filopodia tips (red arrowheads), while EGFP-M15 (jd) and EGFP-M15 (sh2) did not.
150 Boxed regions are magnified (inverted grayscale). **C)** CL4 cells were transfected with EGFP-tagged
151 *Myo15-2* and prepared as above. Both EGFP-M15 (wt) and EGFP-M15 (jd) concentrated at microvillar
152 tips, while EGFP-M15 (sh2) did not. Orthogonal projections are shown (inverted grayscale). Images are
153 representative from at least three independent experiments. Scale bars, 2 µm (A); 20 µm (B+C).

154

155

156 **FIGURE 5**

157 **A)** Cartoon of MYO15 motor domains expressed in *Sf*9 cells, consisting of the ATPase and two light
158 chain binding domains (LCBD). **B)** Size exclusion chromatography analysis of FLAG/IEX purified
159 M15(wt) and M15(jd) proteins. M15(sh2) elutes close to the void volume (arrow) and was aggregated.
160 Protein calibration standards (dotted lines), FLAG peptide (asterisk). **C)** SDS-PAGE analysis of SEC
161 purified motor domain proteins. The motor domain (arrow) co-purifies with RLC and ELC light chains
162 for all variants. M15(sh2) was misfolded and extracted from *Sf*9 cells at low yield. **D)** Steady-state
163 ATPase activation of M15(wt) and M15(jd) motor domains measured using a NADH-coupled assay at
164 20 ± 0.1°C. Reactions were performed with [F-actin] as shown. Rectangular hyperbola fits are shown
165 for M15(wt) (blue, k_{cat} = 5.8 ± 0.2 s^{-1}, k_{ATPase} = 29.1 ± 2.1 µM) and for M15(jd) (green, k_{cat} = 0.87 ± 0.04
166 s^{-1}, k_{ATPase} = 114.3 ± 8.2 µM, n = 4). **E)** Frequency histogram of F-actin velocities in a gliding filament
167 assay at 30 ± 0.1°C. Gaussian fits (dotted line) are overlaid for M15(wt) (473 ± 67 nm·s^{-1}, n = 5449

168 filaments, mean ± SD) and M15(jd) (216 ± 71 nm·s^{-1}, n = 2844 filaments). Data are from 2
169 independent experiments.
170
171
172 **FIGURE 6**
173 **A)** Fluorescent time-course of 2 μM G-actin (10% pyrene) measured in a fluorimeter (red trace).
174 Polymerization was induced by addition of KMEI (1x) at t = 0 s. Introduction of 1 μM M15(wt) (blue) at t
175 = 0 s increases in actin polymerization following an inflexion point (arrow), whilst 1 μM M15(jd) (green)
176 does not (arrow). Reactions contains 70 μM ATP carried over from the actin storage G-buffer. **B)** First
177 derivative of pyrene fluorescence with respect to time for G-actin + M15(wt)(blue) and G-actin +
178 M15(jd)(green). **C)** Fluorescent time course of 2 μM G-actin (10% pyrene) induced to polymerize by
179 KMEI buffer in the absence of free ATP (red trace). G-actin monomers were desalted immediately
180 prior to use, ensuring they were ATP bound. Addition of 1 μM M15(wt) (blue) triggers an almost
181 immediate increase in actin polymerization. **D)** Quantification of time to reach half maximal
182 fluorescence (n = 4).
183
184
185 **FIGURE 7**
186 **A)** TIRFM visualization of actin filaments polymerizing on PEG-biotin-neutravidin functionalized cover
187 glass. Polymerization of 1 μM G-actin (20% TMR + 10% biotin labelled) was induced by 1 x KMEI (50
188 mM KCl, 1 mM $MgCl_2$, 1 mM EGTA, 10 mM imidazole, pH 7.0) at t = 0 s, in the presence of 25 μM ATP.
189 Representative time-lapses shown for: 1 μM G-actin (top), 1 μM G-actin + 1 μM M15(wt) (middle), and
190 1 μM G-actin + 1 μM mutant M15(jd) (bottom). **B)** Quantification of actin filament density shows delayed
191 nucleation activity of MYO15 in the presence of ATP. **C)** Kymographs of actin filament elongation. **D**)
192 Barbed end elongation rates for G-actin alone (red), G-actin + M15(wt) (blue), G-actin + M15(jd) (green).
193 **E + F)** Elongation rate data (from D) re-binned as before (E), or after (F) nucleation. The G-actin + KMEI
194 control data set (from D) is reproduced identically as a comparator in E and F. **G)** Time-lapse of actin
195 filaments polymerization induced by KMEI at t = 0 s, with no ATP in solution. G-actin (ATP) monomers
196 were prepared by desalting into ATP-free G-buffer. **H)** Actin filament density shows nucleation activity
197 of MYO15 is accelerated in the absence of ATP. **I)** Barbed end filament rates in the absence of free
198 ATP. Reaction deadtimes were typically 50 s and included in quantification. TIRFM images are shown
199 as inverted grayscale. Scale bars are 10 μm (A,G). Data are from 4 experiments, using 2 independent
200 protein preparations.
201

202

203 **FIGURE S1**

204 **A)** Whole genome SNP mapping of genomic DNA from ten MPC190 mice exhibiting hearing loss (red,
205 HL) and three hearing (H) littermate controls. The genotype of each mouse is either homozygous for
206 C57BL/6J (black box), C3H (white box) or heterozygous (grey box) for each marker. The analysis
207 defined a 16.5Mb critical interval on Chromosome 11 between markers rs29410974 and rs26906764
208 (Chr11:50420012-67162951, GRCm38). **B)** Sanger sequencing confirmed the only WGS-identified,
209 coding lesion (arrow) within the critical interval, in exon 17 (ENSMUSE00000244718) of the *Myo15*
210 gene (ENSMUSG00000042678). A nucleotide transition (c.4940A>G) at codon 1647 alters the wild-
211 type aspartate (D) codon to a mutant glycine (G). Example electropherograms are shown for *Myo15*$^{+/+}$,
212 *Myo15*$^{+/jd}$ and *Myo15*$^{jd/jd}$. **C-F)** Minimum ABR detection thresholds for a longitudinal cohort of *Myo15*$^{jd/jd}$
213 mice (n = 10), *Myo15*$^{+/+}$ (n=10) and *Myo15*$^{+/jd}$ (n=15) littermates at 4, 6, 9 and 12 weeks reveal
214 progressive hearing loss. Data points represent individual mice, with the mean value indicated. **** p
215 < 0.0001; two-way ANOVA with Tukey's multiple comparisons test. **G)** Distortion Product Otoacoustic
216 Emission (DPOAE) responses are greatly reduced at 12 weeks in *Myo15*$^{jd/jd}$ mutants (red, n = 10) at
217 all frequencies tested compared with *Myo15*$^{+/+}$ (black, n = 9) and *Myo15*$^{+/jd}$ (gray, n = 14) littermates.
218 Data are mean ± SD.

219

220

221 **FIGURE S2**

222 **A)** SEM analyses of IHC bundles from *Myo15*$^{jd/jd}$ and *Myo15*$^{+/+}$ littermates at 12 weeks. **B)**
223 Quantification of the tallest (row 1) stereocilia at 12 weeks in IHCs from *Myo15*$^{+/+}$ mice (45 stereocilia
224 from 3 animals) and *Myo15*$^{jd/jd}$ mice (45 stereocilia from 3 animals). **** $p < 0.0001$, unpaired, two-
225 tailed *t*-test. **C)** SEM analyses of *Myo15*$^{jd/jd}$ OHC bundles at 12 weeks. OHC bundles were qualitatively
226 categorized as "intact", "abnormal/damaged" or "missing". Representative examples are shown. In the
227 "abnormal/damaged" group, stereocilia were typically resorbed from the periphery of the hair bundle.
228 **D)** Quantification of OHC bundle categories at 12 weeks in *Myo15*$^{+/+}$ (1344 OHCs from 4 animals) and
229 *Myo15*$^{jd/jd}$ littermates (972 OHCs from 4 animals). All images and quantification are from the mid-
230 cochlear turn. Scale bars, 1 μm.

231

232

233 **FIGURE S3**

234 Immunofluorescence (IF) confocal images of anti-EPS8, anti-WHRN, anti-GNAI3 labelling or anti-
235 GPSM2 (green) in control *Myo15*$^{+/jd}$ and *Myo15*$^{jd/jd}$ IHCs fixed at P14. Phalloidin was used to label F-

236 actin (magenta). Images are representative of data from two independent animals per genotype and
237 antibody combination. Scale bars, 10 μm.
238

FIGURE 1

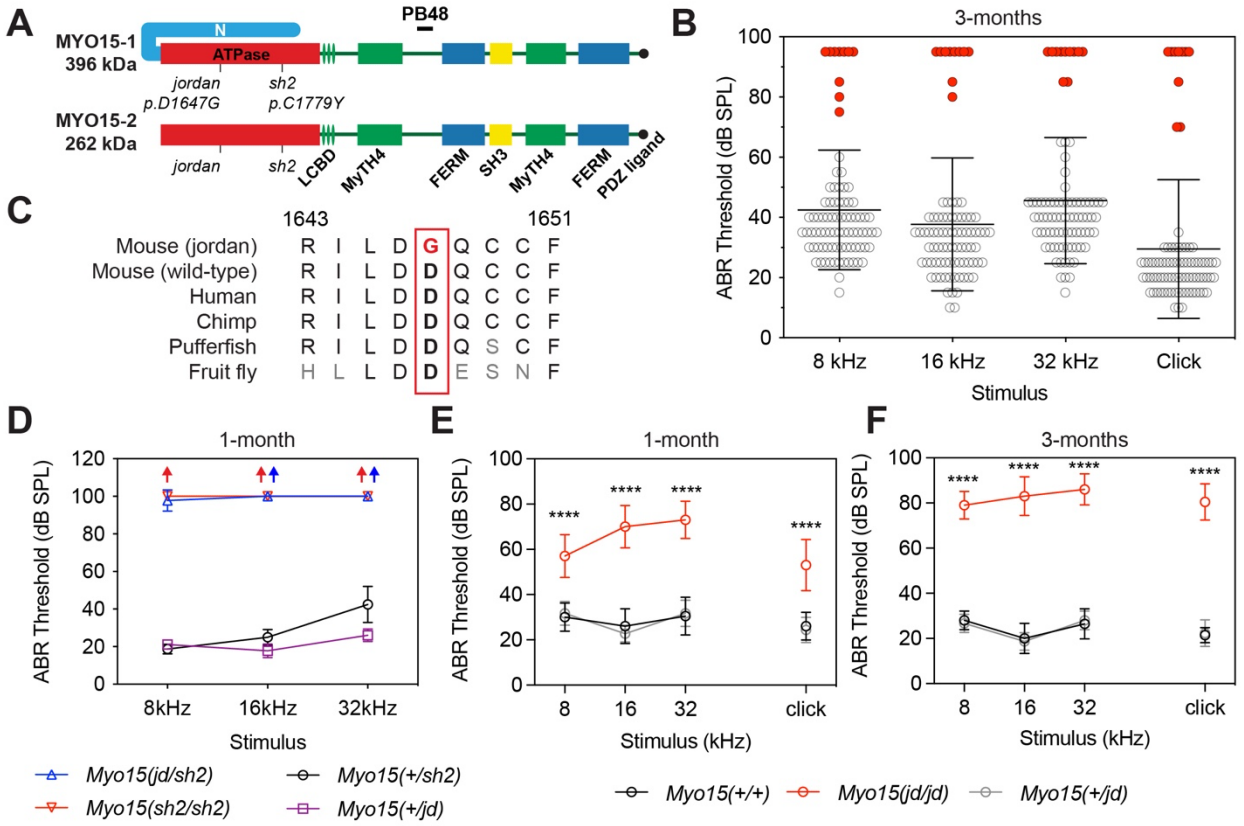
A
MYO15-1
396 kDa
N
ATPase
PB48
jordan
p.D1647G
sh2
p.C1779Y
MYO15-2
262 kDa
jordan
sh2
LCBD
MyTH4
FERM
SH3
MyTH4
FERM
PDZ ligand
B
3-months
ABR Threshold (dB SPL)
8 kHz
16 kHz
32 kHz
Click
Stimulus
C
1643
1651
Mouse (jordan) R I L D G Q C C F
Mouse (wild-type) R I L D D Q C C F
Human R I L D D Q C C F
Chimp R I L D D Q C C F
Pufferfish R I L D D Q S C F
Fruit fly H L L D D E S N F
D
1-month
ABR Threshold (dB SPL)
8kHz
16kHz
32kHz
Stimulus
Myo15(jd/sh2)
Myo15(+/sh2)
Myo15(sh2/sh2)
Myo15(+/jd)
E
1-month
ABR Threshold (dB SPL)
8
16
32
click
Stimulus (kHz)
F
3-months
ABR Threshold (dB SPL)
8
16
32
click
Stimulus (kHz)
Myo15(+/+)
Myo15(jd/jd)
Myo15(+/jd)

FIGURE 2

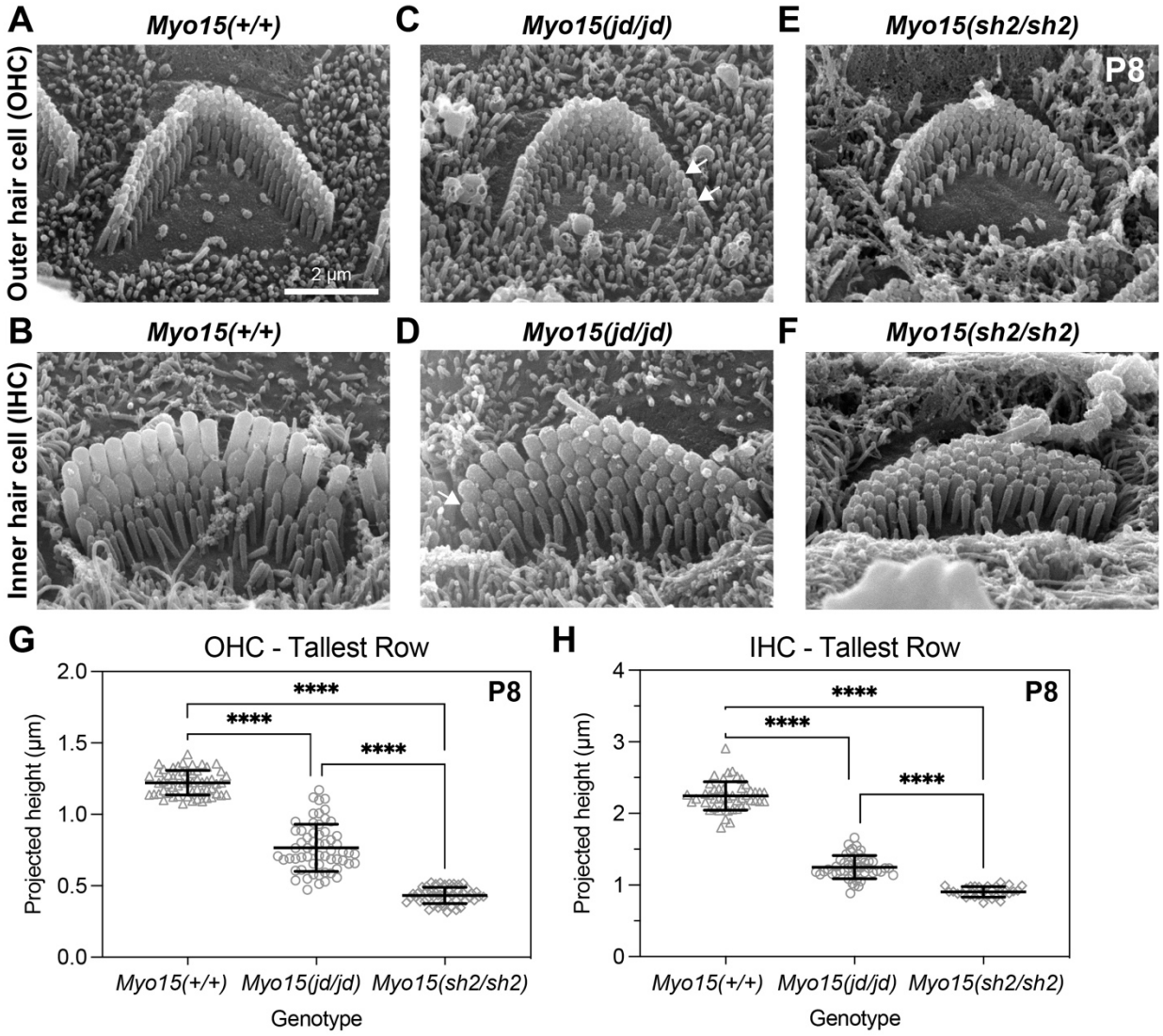
A
Myo15(+/+)
C
Myo15(jd/jd)
E
Myo15(sh2/sh2)
P8
Outer hair cell (OHC)
2 µm
B
Myo15(+/+)
D
Myo15(jd/jd)
F
Myo15(sh2/sh2)
Inner hair cell (IHC)
G
OHC - Tallest Row
P8
****
****
****
Projected height (µm)
2.0
1.5
1.0
0.5
0.0
Myo15(+/+)
Myo15(jd/jd)
Myo15(sh2/sh2)
Genotype
H
IHC - Tallest Row
P8
****
****
****
Projected height (µm)
4
3
2
1
0
Myo15(+/+)
Myo15(jd/jd)
Myo15(sh2/sh2)
Genotype

FIGURE 3

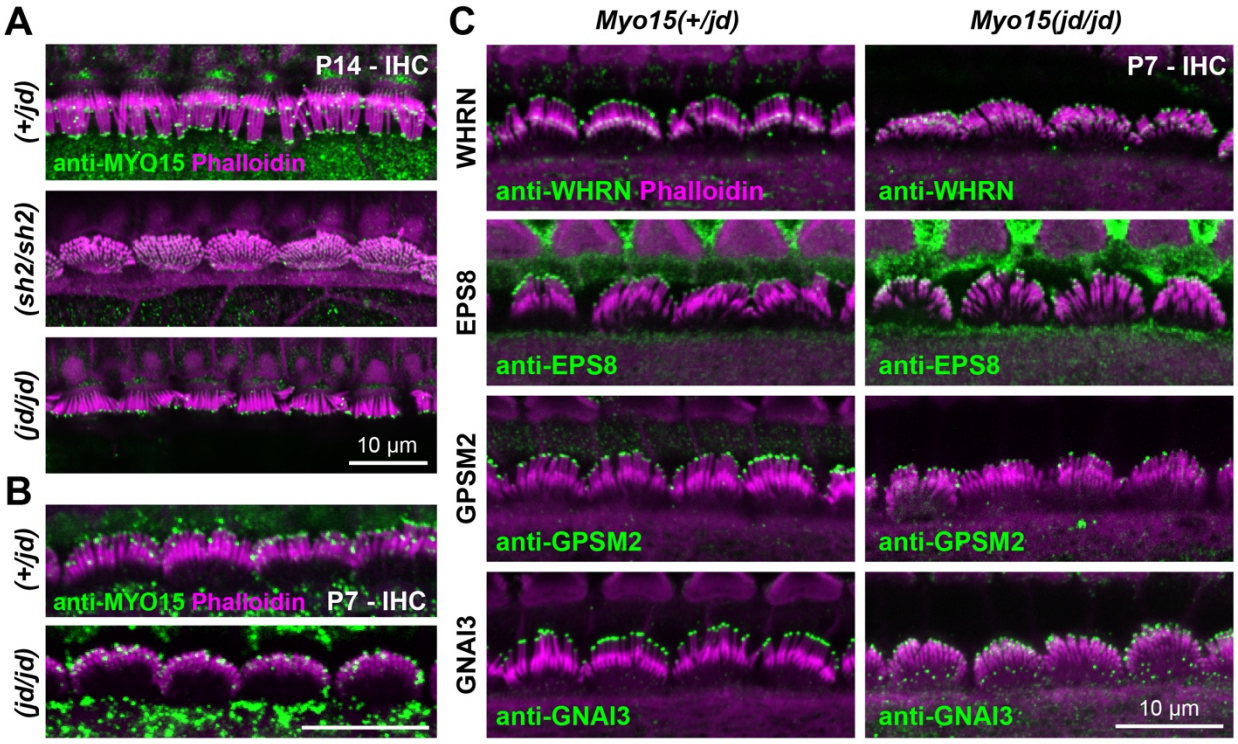
A
P14 - IHC
(+/jd)
anti-MYO15 Phalloidin
(sh2/sh2)
(jd/jd)
10 µm
B
(+/jd)
anti-MYO15 Phalloidin
P7 - IHC
(jd/jd)
C
Myo15(+/jd)
Myo15(jd/jd)
WHRN
anti-WHRN Phalloidin
P7 - IHC
anti-WHRN
EPS8
anti-EPS8
anti-EPS8
GPSM2
anti-GPSM2
anti-GPSM2
GNAI3
anti-GNAI3
anti-GNAI3
10 µm

FIGURE 4

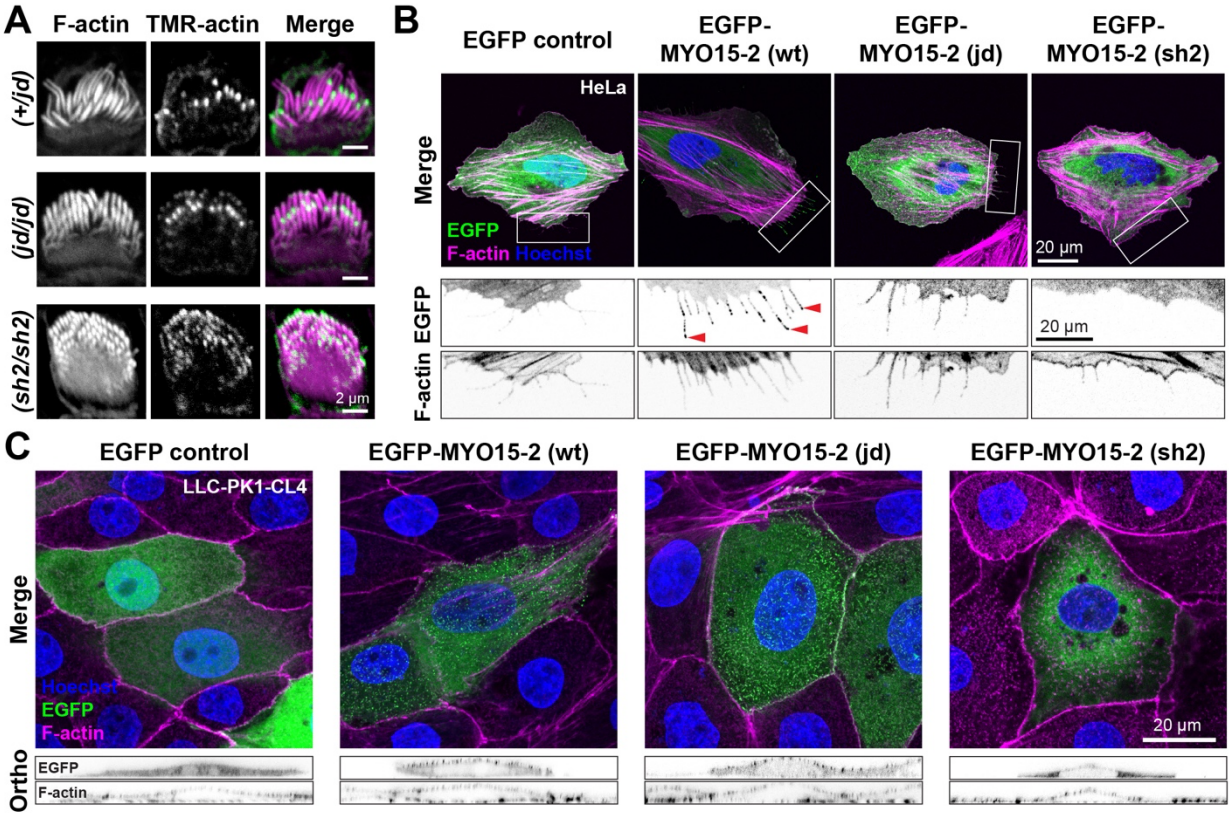
A
F-actin
TMR-actin
Merge
(+/jd)
(jd/jd)
(sh2/sh2)
2 µm
B
EGFP control
EGFP-MYO15-2 (wt)
EGFP-MYO15-2 (jd)
EGFP-MYO15-2 (sh2)
HeLa
Merge
EGFP
F-actin Hoechst
20 µm
EGFP
F-actin
20 µm
C
EGFP control
EGFP-MYO15-2 (wt)
EGFP-MYO15-2 (jd)
EGFP-MYO15-2 (sh2)
LLC-PK1-CL4
Merge
Hoechst
EGFP
F-actin
20 µm
Ortho
EGFP
F-actin

FIGURE 5

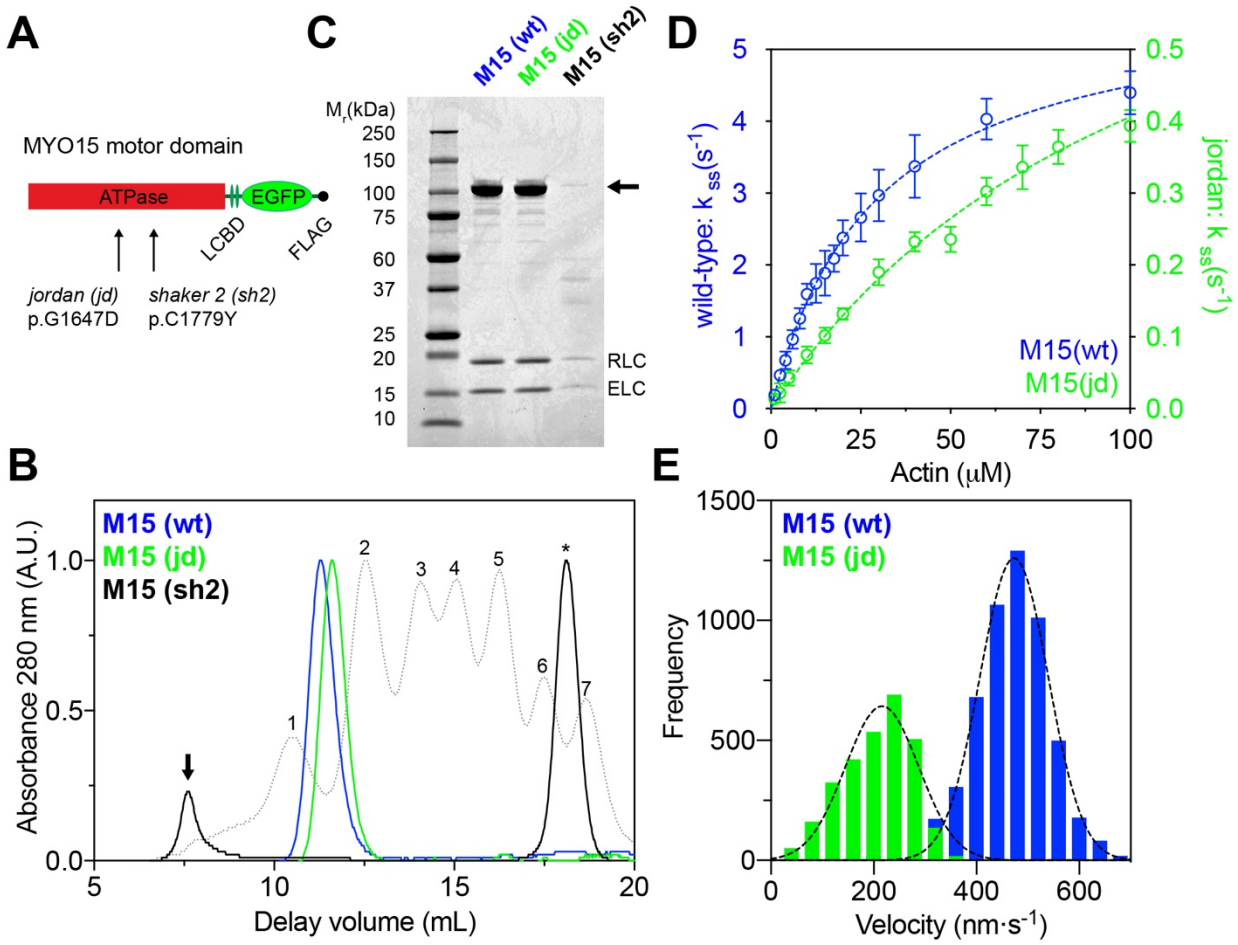
A
MYO15 motor domain
ATPase
EGFP
LCBD
FLAG
jordan (jd)
p.G1647D
shaker 2 (sh2)
p.C1779Y
C
M15 (wt)
M15 (jd)
M15 (sh2)
Mr(kDa)
250
150
100
75
60
37
25
20
15
10
RLC
ELC
D
wild-type: kss(s-1)
jordan: kss(s-1)
M15(wt)
M15(jd)
Actin (μM)
B
M15 (wt)
M15 (jd)
M15 (sh2)
Absorbance 280 nm (A.U.)
Delay volume (mL)
E
M15 (wt)
M15 (jd)
Frequency
Velocity (nm·s-1)

FIGURE 6

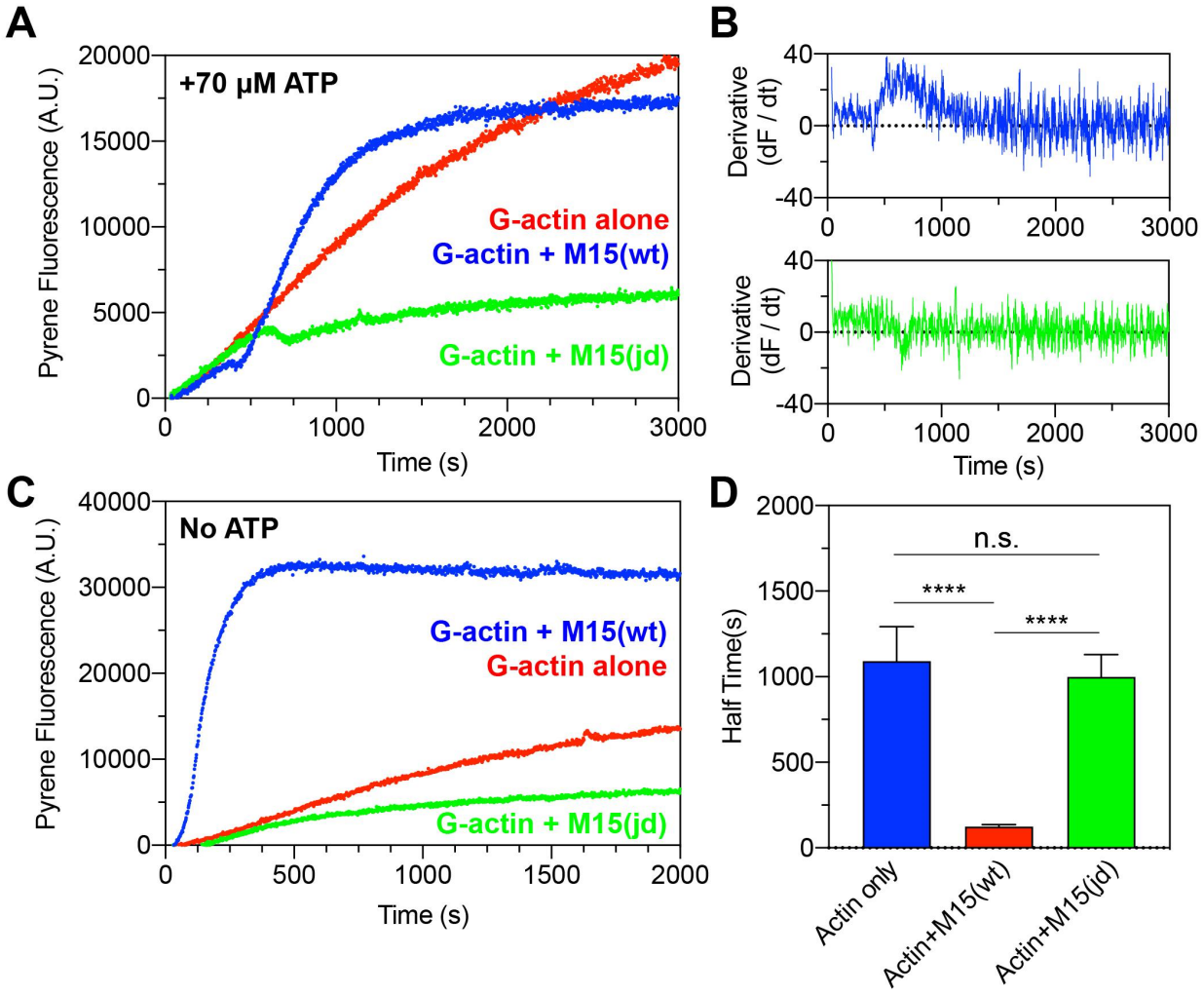
A
+70 μM ATP
Pyrene Fluorescence (A.U.)
Time (s)
G-actin alone
G-actin + M15(wt)
G-actin + M15(jd)
B
Derivative (dF / dt)
Time (s)
C
No ATP
Pyrene Fluorescence (A.U.)
Time (s)
G-actin + M15(wt)
G-actin alone
G-actin + M15(jd)
D
Half Time(s)
n.s.
****
****
Actin only
Actin+M15(wt)
Actin+M15(jd)

FIGURE 7

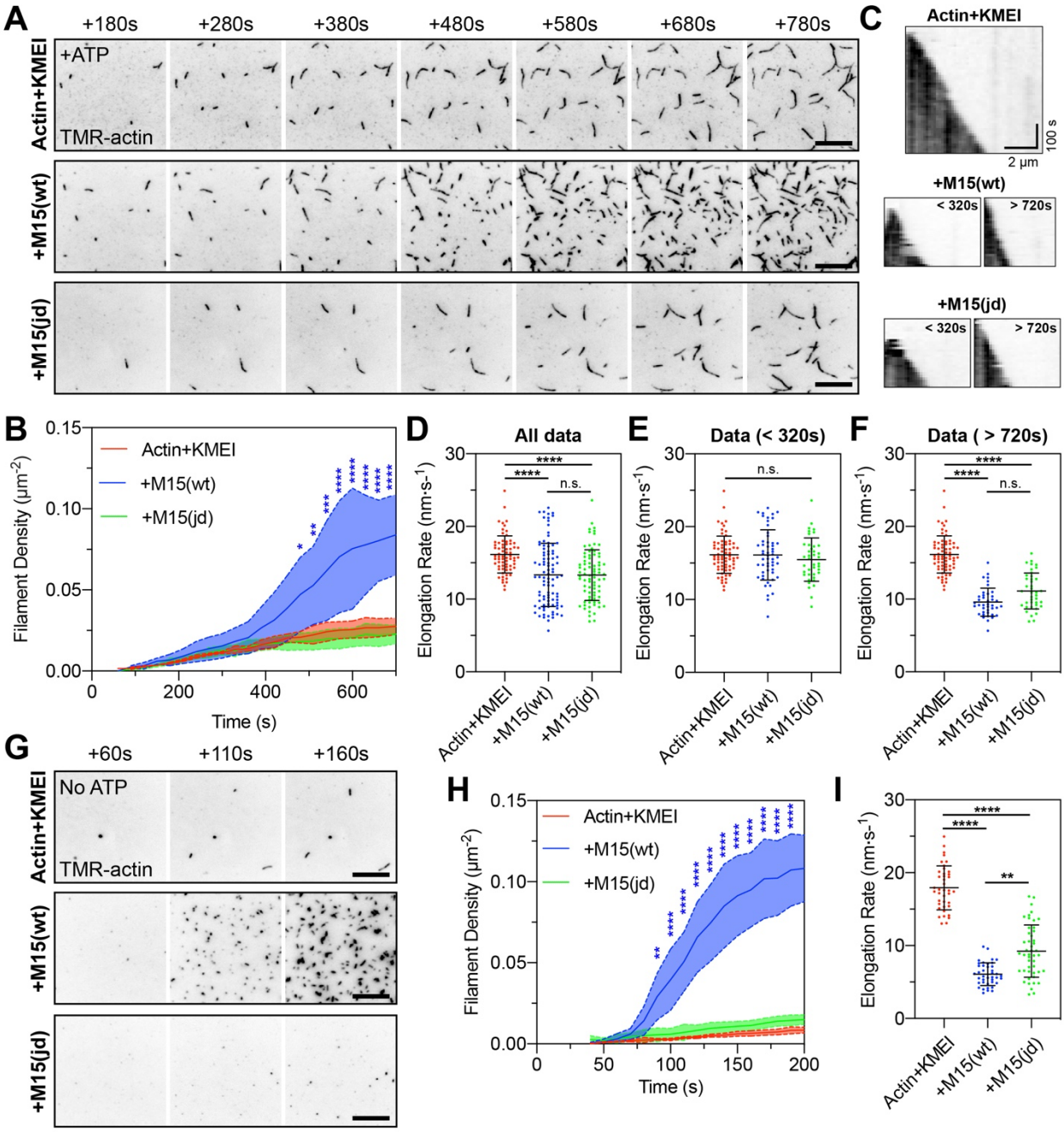
A
+180s
+280s
+380s
+480s
+580s
+680s
+780s
Actin+KMEI
+ATP
TMR-actin
+M15(wt)
+M15(jd)
C
Actin+KMEI
100 s
2 µm
+M15(wt)
< 320s
> 720s
+M15(jd)
< 320s
> 720s
B
Actin+KMEI
+M15(wt)
+M15(jd)
Filament Density (µm-2)
Time (s)
D
All data
E
Data (< 320s)
F
Data (> 720s)
Elongation Rate (nm·s-1)
n.s.
Actin+KMEI
+M15(wt)
+M15(jd)
G
+60s
+110s
+160s
No ATP
TMR-actin
H
I

FIGURE S1

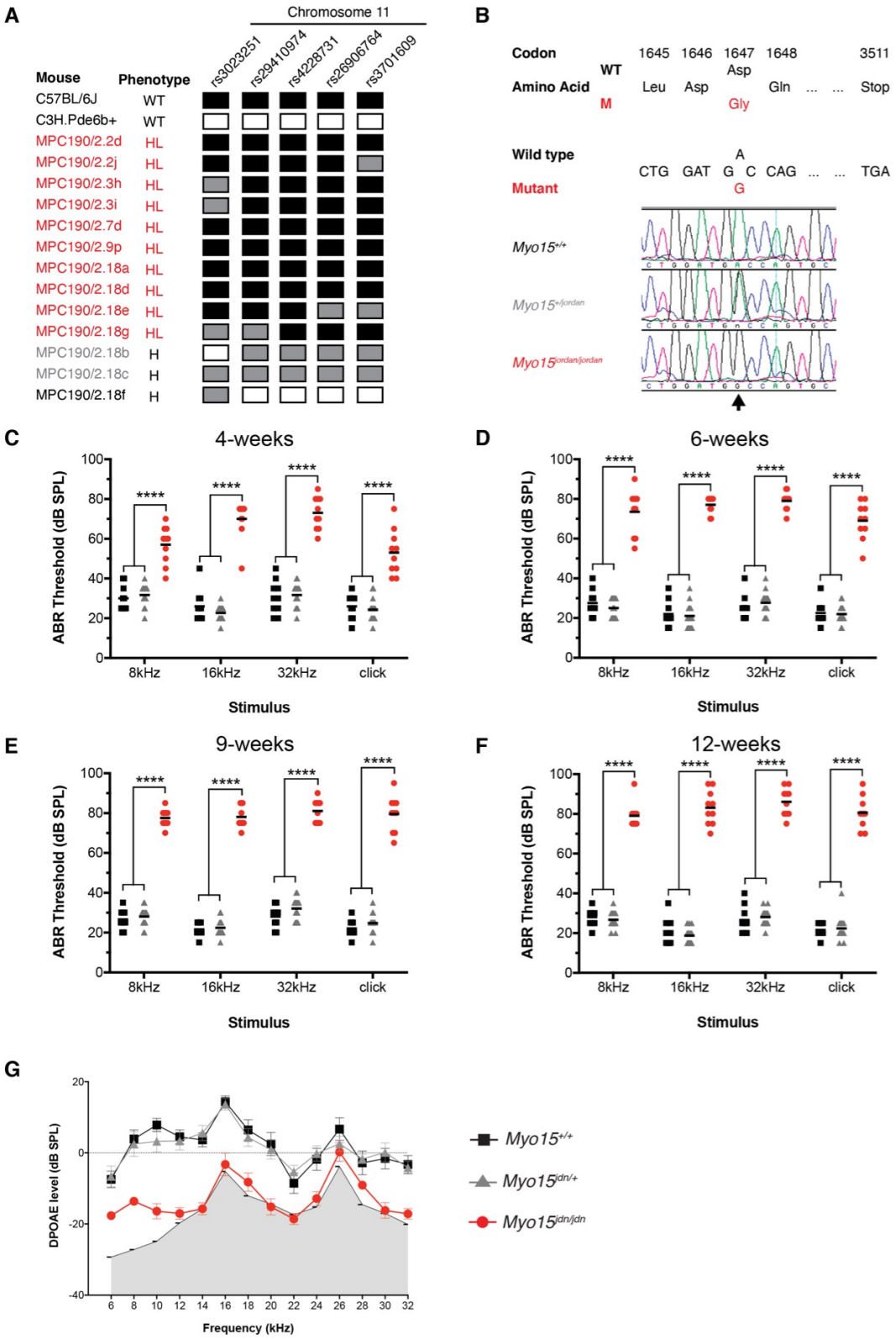
A
Chromosome 11
rs3023251
rs29410974
rs4228731
rs26906764
rs3701609
Mouse
Phenotype
C57BL/6J WT
C3H.Pde6b+ WT
MPC190/2.2d HL
MPC190/2.2j HL
MPC190/2.3h HL
MPC190/2.3i HL
MPC190/2.7d HL
MPC190/2.9p HL
MPC190/2.18a HL
MPC190/2.18d HL
MPC190/2.18e HL
MPC190/2.18g HL
MPC190/2.18b H
MPC190/2.18c H
MPC190/2.18f H
B
Codon
1645 1646 1647 1648 3511
WT
Asp
Amino Acid
Leu Asp Gln ... ... Stop
M
Gly
Wild type
A
CTG GAT G C CAG ... ... TGA
Mutant
G
Myo15+/+
Myo15+/jordan
Myo15jordan/jordan
C
4-weeks
D
6-weeks
E
9-weeks
F
12-weeks
ABR Threshold (dB SPL)
8kHz
16kHz
32kHz
click
Stimulus
****
G
DPOAE level (dB SPL)
Frequency (kHz)
Myo15+/+
Myo15jdn/+
Myo15jdn/jdn

FIGURE S2

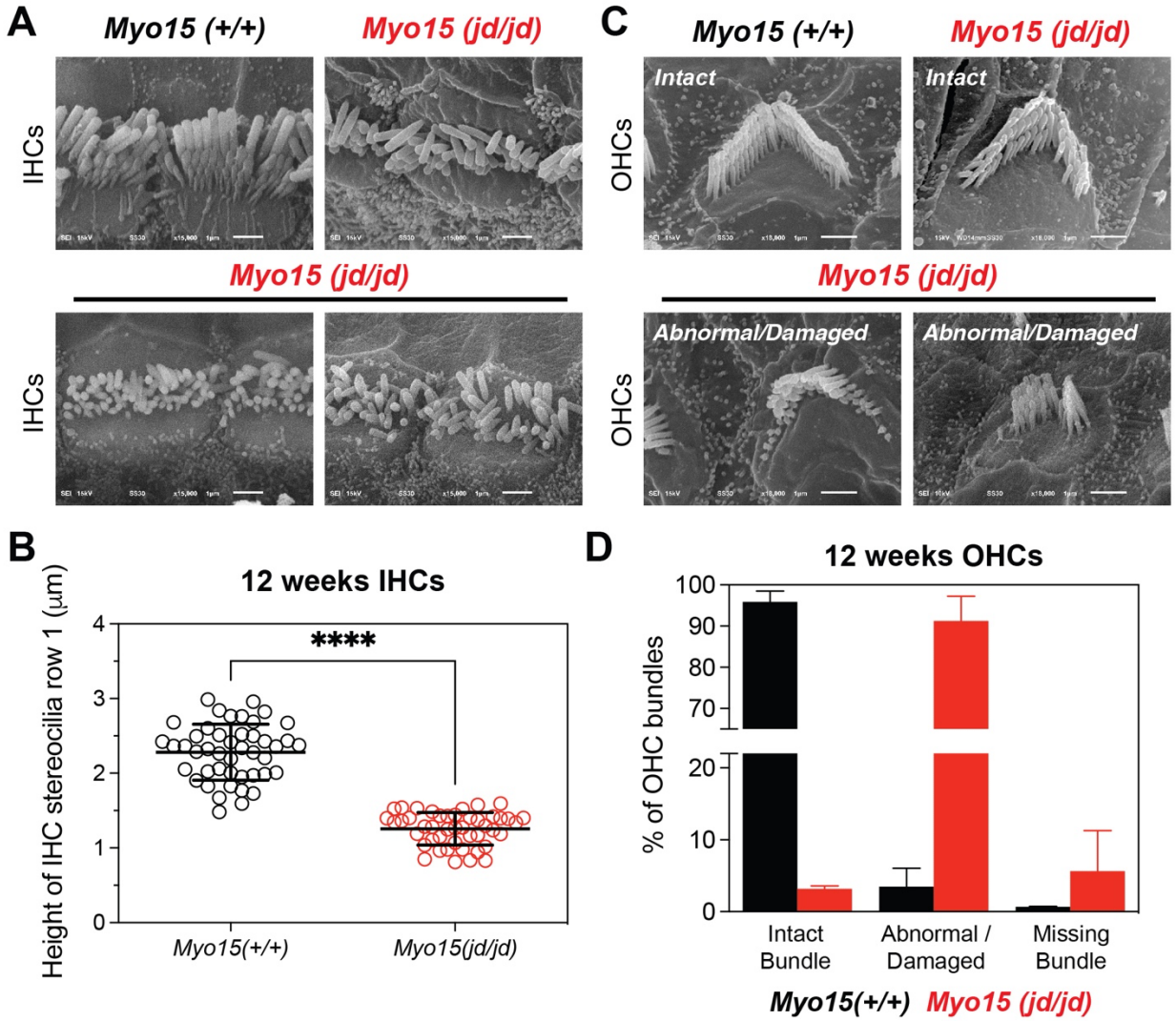
A
Myo15 (+/+)
Myo15 (jd/jd)
IHCs
Myo15 (jd/jd)
IHCs
C
Myo15 (+/+)
Myo15 (jd/jd)
OHCs
Intact
Intact
Myo15 (jd/jd)
OHCs
Abnormal/Damaged
Abnormal/Damaged
B
12 weeks IHCs
Height of IHC stereocilia row 1 (μm)
****
0
1
2
3
4
Myo15(+/+)
Myo15(jd/jd)
D
12 weeks OHCs
% of OHC bundles
100
90
80
70
20
10
0
Intact Bundle
Abnormal / Damaged
Missing Bundle
Myo15(+/+)
Myo15 (jd/jd)

FIGURE S3

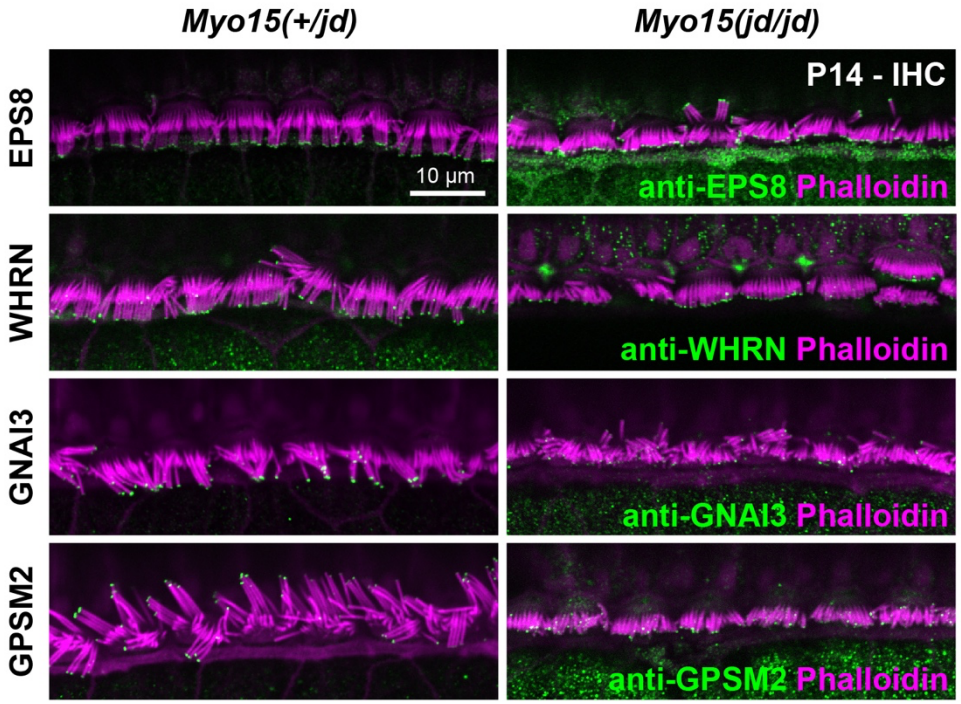
Myo15(+/jd)
Myo15(jd/jd)
EPS8
WHRN
GNAI3
GPSM2
P14 - IHC
10 µm
anti-EPS8 Phalloidin
anti-WHRN Phalloidin
anti-GNAI3 Phalloidin
anti-GPSM2 Phalloidin